



# Carbonate facies-specific stable isotope data record climate, hydrology, and microbial communities in Great Salt Lake, UT

Miquela Ingalls<sup>1,2</sup> | Carie M. Frantz<sup>3</sup> | Kathryn E. Snell<sup>1</sup> | Elizabeth J. Trower<sup>1</sup>

<sup>1</sup>Department of Geological Sciences, University of Colorado, Boulder, CO, USA

<sup>2</sup>Division of Geological and Planetary Sciences, California Institute of Technology, Pasadena, CA, USA

<sup>3</sup>Department of Earth & Environmental Sciences, Weber State University, Ogden, UT, USA

## Correspondence

Miquela Ingalls, Department of Geological Sciences, University of Colorado, Boulder, CO 80309, USA.

Email: mingalls@caltech.edu

## Funding information

Division of Earth Sciences, Grant/Award Number: 1826850 and 1826869; Barr Foundation

## Abstract

Organic and inorganic stable isotopes of lacustrine carbonate sediments are commonly used in reconstructions of ancient terrestrial ecosystems and environments. Microbial activity and local hydrological inputs can alter porewater chemistry (e.g., pH, alkalinity) and isotopic composition (e.g.,  $\delta^{18}\text{O}_{\text{water}}$ ,  $\delta^{13}\text{C}_{\text{DIC}}$ ), which in turn has the potential to impact the stable isotopic compositions recorded and preserved in lithified carbonate. The fingerprint these syngenetic processes have on lacustrine carbonate facies is yet unknown, however, and thus, reconstructions based on stable isotopes may misinterpret diagenetic records as broader climate signals. Here, we characterize geochemical and stable isotopic variability of carbonate minerals, organic matter, and water within one modern lake that has known microbial influences (e.g., microbial mats and microbialite carbonate) and combine these data with the context provided by 16S rRNA amplicon sequencing community profiles. Specifically, we measure oxygen, carbon, and clumped isotopic compositions of carbonate sediments ( $\delta^{18}\text{O}_{\text{carb}}$ ,  $\delta^{13}\text{C}_{\text{carb}}$ ,  $\Delta_{47}$ ), as well as carbon isotopic compositions of bulk organic matter ( $\delta^{13}\text{C}_{\text{org}}$ ) and dissolved inorganic carbon (DIC;  $\delta^{13}\text{C}_{\text{DIC}}$ ) of lake and porewater in Great Salt Lake, Utah from five sites and three seasons. We find that facies equivalent to ooid grainstones provide time-averaged records of lake chemistry that reflect minimal alteration by microbial activity, whereas microbialite, intraclasts, and carbonate mud show greater alteration by local microbial influence and hydrology. Further, we find at least one occurrence of  $\Delta_{47}$  isotopic disequilibrium likely driven by local microbial metabolism during authigenic carbonate precipitation. The remainder of the carbonate materials (primarily ooids, grain coatings, mud, and intraclasts) yield clumped isotope temperatures ( $T(\Delta_{47})$ ),  $\delta^{18}\text{O}_{\text{carb}}$ , and calculated  $\delta^{18}\text{O}_{\text{water}}$  in isotopic equilibrium with ambient water and temperature at the time and site of carbonate precipitation. Our findings suggest that it is possible and necessary to leverage diverse carbonate facies across one sedimentary horizon to reconstruct regional hydroclimate and evaporation–precipitation balance, as well as identify microbially mediated carbonate formation.

## KEY WORDS

carbonate, clumped isotopes, facies analysis, microbialite, ooid, sedimentology

## 1 | INTRODUCTION

The relative abundance and distribution of carbon and oxygen stable isotopes within carbonate lake sediments and organic matter are commonly used to reconstruct physicochemical conditions in ancient terrestrial environments (e.g., temperature, aridity, elevation, and vegetation; e.g., Leng & Marshall, 2004). Carbonate carbon and oxygen are derived from the chemical constituents of the water from which they precipitate. Carbonate oxygen isotope composition ( $\delta^{18}\text{O}_{\text{carb}}$ ) is determined by the oxygen isotope composition of the water and the temperature of mineral formation (O'Neil, Clayton, & Mayeda, 1969). For this reason,  $\delta^{18}\text{O}_{\text{carb}}$  is often used to glean paleoclimate and paleoenvironmental information, such as land surface temperatures, regional climate, and hydrology of ancient carbonate-forming basins. Carbonate carbon isotope composition ( $\delta^{13}\text{C}$ ) is primarily determined by water dissolved inorganic carbon (DIC), which derives carbon from atmospheric  $\text{CO}_2$  (presently  $\sim 8\%$  vs. VPDB) and oxidized organic matter (a range of compositions). However, many biotic and chemical processes can alter the concentration and isotopic composition of carbon preserved in the sedimentary record prior to lithification. Understanding the fractionations associated with these reactions allows us to better understand the rates and mechanisms of biological and geochemical carbon cycling in modern aqueous environments. However, DIC and a large fraction of organic carbon are lost from the system by syngenetic processes such as mineralization, degradation, and metabolism. Thus, our primary record of ancient carbon is in carbonate minerals. As such, we require an understanding of how the processes that set the isotopic compositions of DIC and organic C are translated to and preserved in carbonate minerals. The goal of our study is to determine when and how hydrology, climate and biology impact the lacustrine carbonate rock record so that isotopic data may be used appropriately to reconstruct biologically and chemically complex systems.

When carbon and oxygen isotopes are used in paleoclimatology and paleolimnology applications, it is typically done with the assumption that these archives record primary information about the environment in which the carbonate minerals precipitated and organic matter synthesized. When samples are measured from a single stratigraphic section, an implicit assumption is that a single horizon is geochemically homogeneous, and thus, the isotopic and geochemical record of change is interpreted as purely external (e.g., climate) rather than a record of internal variability (e.g., local processes and inputs). Previous studies have documented the  $\delta^{18}\text{O}_{\text{carb}}$  and  $\delta^{13}\text{C}_{\text{carb}}$  of a variety of carbonate sediments from the shorelines of Great Salt Lake (GSL) that date back to the time of Lake Bonneville (~30 to 11 ka; Oviatt, 2015). Positive correlation between  $\delta^{18}\text{O}_{\text{carb}}$  and  $\delta^{13}\text{C}_{\text{carb}}$  is found in hydrologically closed basin lakes (Figure 6a; Lettéron et al., 2018; Li & Ku, 1997; Martin-Bello, Arenas, Andrews, Alonso-Zarza, & Marca, 2019; Talbot, 1990) such as GSL. It is thought that  $\delta^{13}\text{C}_{\text{DIC}}$  increases during intervals of lake level drop due to increased primary productivity by cyanobacteria and algae (Leng & Marshall, 2004). The increase in primary productivity has been linked to warmer temperatures and an increased net

concentration of nutrients in the near surface due to total reduction in lake volume and upwelling of nutrient-rich bottom waters (Li & Ku, 1997). Organic matter preferentially uptakes  $^{12}\text{C}$ , leaving behind water DIC enriched in  $^{13}\text{C}$ . Meanwhile, when lake levels drop due to lower recharge rates and increased evaporation,  $^{16}\text{O}$  is preferentially removed into the vapor phase by Rayleigh fractionation, thereby increasing the  $^{18}\text{O}/^{16}\text{O}$  ratios in the residual lakewater (Dansgaard, 1964; Kelts & Talbot, 1990). Therefore, we expect a notable positive  $\delta^{13}\text{C}_{\text{carb}}-\delta^{18}\text{O}_{\text{carb}}$  correlation in carbonate facies that are sensitive to hydroclimate, with higher  $^{13}\text{C}/^{12}\text{C}$  and  $^{18}\text{O}/^{16}\text{O}$  ratios in carbonate sediments deposited during intervals of GSL water level recession and lower during intervals of transgression due to dilution with the lighter isotopes.

In this work, we investigate how and the magnitude by which localized microbial activity and hydrological inputs can obscure the broader climatic and environmental signal in carbonate lake sediments. We measure stable isotope ratios of inorganic and organic carbon pools within GSL (oids, microbialite carbonate, microbialite intraclasts, carbonate mud, water DIC, and organic matter) and characterize the spatiotemporal variability in these records across a north-south extent of shoreline carbonate facies from the modern and last several thousand years. We determine which carbonate facies are more sensitive to changes in water chemistry from hydrological inputs or localized microbial metabolisms in subsurface communities by pairing 16S rRNA sequencing with organic and inorganic stable isotope measurements, and determine potential isotopic, geochemical, and mineralogical signatures for these early diagenetic processes as they may be recorded in the rock record.

### 1.1 | Geologic setting

Modern GSL's basin geometry and water level evolved via tectonics and climate change in the Cenozoic and, more recently, human activity. GSL is a hypersaline, closed basin lake that represents a vestige of Pleistocene Lake Bonneville. Several lake systems developed in depressions in the Great Basin Province (western USA) formed by crustal extension and collapse from the middle Eocene to early Miocene (49–20 Ma) and later extension from the middle Miocene to present (17 Ma to present; Mohapatra & Johnson, 1998). In the Plio-Pleistocene, water levels of Lake Bonneville and Lake Lahontan experienced transgressive-regressive periods in response to glacial-interglacial cycles (Benson, Currey, Lao, & Hostetler, 1992; Oviatt, 1997, 2015), thereby varying the size, depth, and chemistry of lake-water and mineral precipitates. It is thought that GSL water levels have ranged from approximately the same lake level (~1,278 m asl) since the last major transgression to as high as ~1,295 m asl in the Gilbert episode during the Younger Dryas (~11.5 to 11.6 ka; Oviatt, 2015). A railroad trestle and causeway constructed across the lake in 1904 divided it into North and South Arms. The trestle section was subsequently replaced with a causeway in 1959 (Figure 1), causing the North and South Arms to become chemically and biologically distinct.

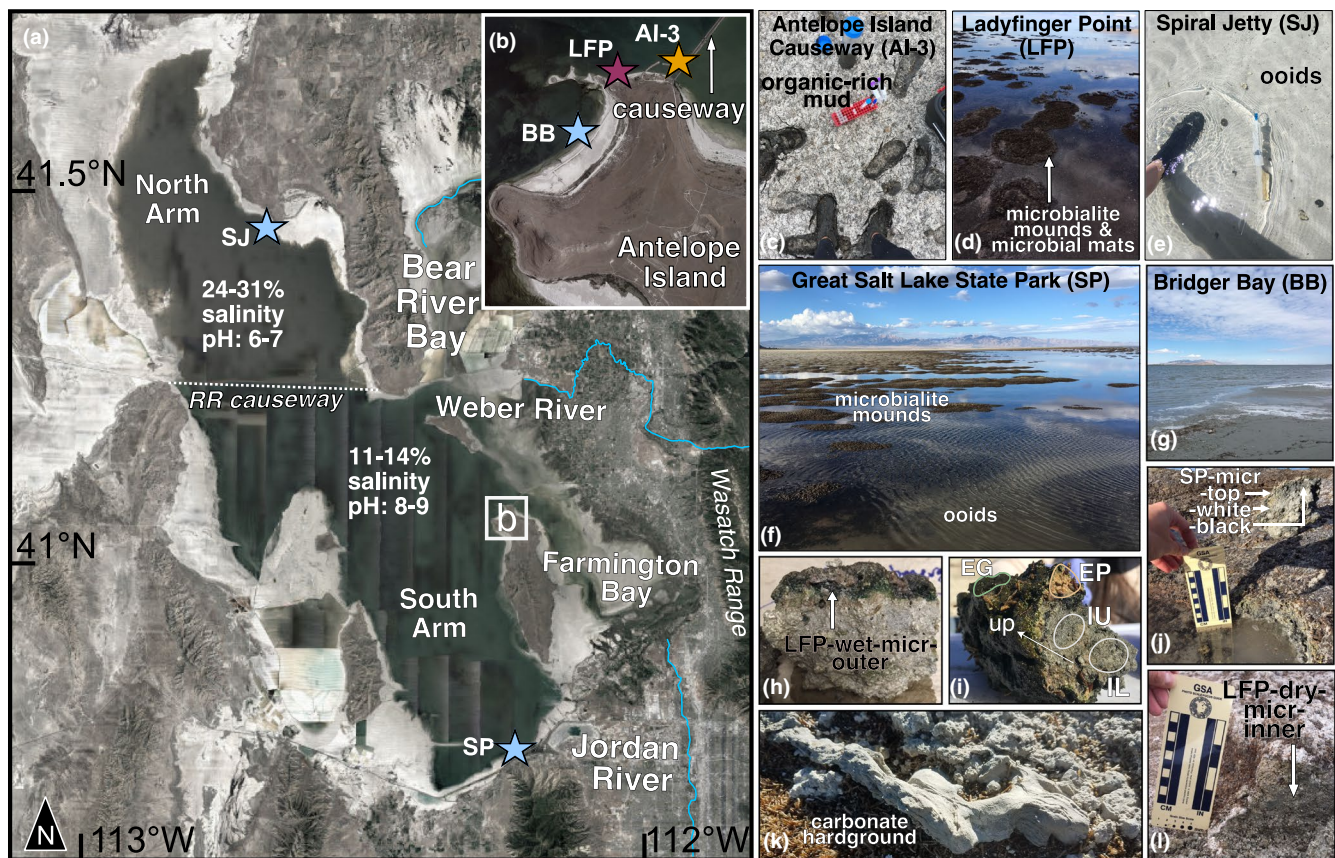


**FIGURE 1** Map of Great Salt Lake adapted from Landsat satellite imagery from December 2016, acquired via Google Earth Pro. Features relevant to hydrology, carbonate chemistry, and biology are labeled. Core sites are marked by stars on (a) the main map and (b) inset of Antelope Island. Light blue stars mark ooid-dominated coring sites. Carbonate from Lady Finger Point (maroon) and the Antelope Island causeway (AI-3; orange) are characterized in text. Site photos with characteristic features are found in panels (c–g). Location of individual microbialite 16S samples are labeled in (h–l), with an example of a hardground from LFP in (k).

Today, GSL is a closed basin lake where water is only removed by evaporation. Because of the shallow shoreline slopes and shallow maximum depth of GSL (<10 m; Baskin & Allen, 2005), even small amounts of lake level change cause relatively large changes in volume and surface area. Surface water flow is the main source of water to GSL, with a very minor groundwater component. The Bear, Weber, and Jordan Rivers are the main freshwater inputs that feed GSL, with source catchments in the Wasatch and Uinta Mountains (Figure 1); however, these rivers only flow into the South Arm. North Arm is hydrologically restricted, meaning the only water input is from rainfall, and therefore, the relative abundance of salts and other ions is controlled entirely by the balance of precipitation and evaporation. North Arm salinity is consistently near saturation of sodium chloride, while the hydrochemistry of the South Arm is balanced by evaporation and inputs from seasonal melts and fluvial freshwater (Rupke & McDonald, 2012).

Ooids, tufas, microbialites, carbonate mud, and micritic grain coatings make up the dominant carbonate components of GSL (Figure 1). Microbialites and calcareous hardgrounds—primarily

composed of cemented ooids and intraclasts—form in association with microbial mats on the shorelines of GSL (Eardley, 1938; Lindsay et al., 2017; Figure 1) and potentially in deeper waters. The distribution of the nearshore domal microbialite mounds has been directly mapped to microtopographic highs on the lake floor related to regional structures, such as the East Lake Fault (Bouton et al., 2016). Minerals and nutrients thought to encourage the growth of microbialites are delivered via seepage of basinal fluids along fault surfaces (Sei & Fathepure, 2009).

Newell, Jensen, Frantz, and Vanden Berg (2017) measured carbon and oxygen isotopes of unconsolidated ooids, as well as microbialites, tufas, and laminated calcareous hardgrounds from the shoreline of GSL. Newell et al. (2017) report calibrated organic carbon  $^{14}\text{C}$  ages of  $10,576 \pm 84$ ,  $10,868 \pm 200$ ,  $12,683 \pm 48$ , and  $7,615 \pm 42$  ka from a core-to-rim transect of a microbialite sample collected at the air-water interface from Buffalo Point on Antelope Island (Newell et al., 2017). Bouton et al. (2016) report uncalibrated  $^{14}\text{C}$  ages of 21,900–2,678 years BP for microbialites from gravity flow deposits on Antelope Island. Sequential leaching of ooids near Antelope Island yield inorganic  $^{14}\text{C}$  ages as old

as ~6,600 years BP, with ~6,000 years of subsequent carbonate accumulation (Paradis et al., 2017).

## 1.2 | Microbiology in Great Salt Lake

Microbial communities that live within lacustrine sediments and colonize microbial mats function in parallel with physicochemical lake properties to determine the structure and composition of authigenic minerals. Microbial mats are commonly characterized by sharp geochemical and redox potential gradients, with diverse communities impacting carbonate chemistry through a variety of metabolic pathways (Dupraz et al., 2009; Dupraz, Visscher, Baumgartner, & Reid, 2004; Visscher & Stolz, 2005). Cyanobacteria fix lake water DIC by oxygenic photosynthesis in the surface layers of mats, thereby locally increasing pH (Dupraz, Fowler, Tobias, & Visscher, 2013). Cyanobacteria also produce extracellular polymeric substances (EPS), which can act as scaffolding for authigenic mineral precipitation and bind the cations necessary for carbonate formation (e.g.,  $\text{Ca}^{2+}$ ,  $\text{Mg}^{2+}$ ; Braissant et al., 2007; Dupraz et al., 2009). Deeper in the anoxic layers of a microbial mat, processes such as anaerobic microbial sulfate reduction and methanogenesis are often responsible for carbon cycling.

The microbiology of GSL has been studied since the 1870s, with great interest paid to the inhabitants of this hypersaline system (Baxter, 2018). Community structure in the stratified water column of the South Arm of the lake is strongly influenced by salinity and dissolved oxygen (Meuser et al., 2013). A link between the microbial community of GSL and carbonate production has long been suspected (Chidsey, Vanden Berg, & Eby, 2015; Lindsay et al., 2017; Pedone & Folk, 1996; Rothpletz, 1892), and recent work has elucidated possible pathways for microbially mediated carbonate production and lithification (e.g., EPS degradation followed by sulfate reduction; Pace et al., 2016) as well as the history of microbial carbonate production and preservation in the Lake Bonneville–GSL system (Bouton et al., 2019). Research related to microbial influences on the geochemical signatures recorded in GSL microbial carbonates has focused on shoreline microbialites (e.g., Newell et al., 2017; Pace et al., 2016). Meanwhile, studies of GSL sediment microbial composition have focused on sulfur and metal cycling, noting the important role played by sulfur-reducing bacteria in GSL sediments (e.g., Boyd et al., 2017).

## 2 | METHODS

Sediment cores, microbialites, and water samples were collected from five sites over three seasons on the shorelines of GSL (Figure 1) for various geochemical, microbiological, and sedimentological analyses. Methodologies are described in brief below, with detailed protocols for sample and data treatment and analytical procedures included in the Appendix S1. A summary of all sample

types collected from each field site and analyses conducted can be found in Table 1.

### 2.1 | Field sampling

Three-inch-diameter sediment push cores were extracted from five near-shore sites (Figure 1; Table 1) in Fall 2017, Spring 2018, and Fall 2018, with Fall and Spring being the endmembers of annual lake level fluctuation. Spiral Jetty (SJ; North Arm), was only sampled in Spring 2018, while all other sites were sampled each season. The southernmost core was taken from GSL State Park (SP) on the southern shore of GSL. Three cores were taken from the northern and western shores of Antelope Island in the South Arm: Bridger Bay (BB), Ladyfinger Point (LFP), and north of the Antelope Island causeway (AI-3). Sections of microbialite mounds were sampled from SP and LFP in Fall 2018 using a chisel and hammer.

We collected filtered lake water and porewater for DIC measurements from each of the five sites in evacuated and acidified (~42%  $\text{H}_3\text{PO}_4$ ) 12-ml round-bottom Labco Exetainer® vials. Porewater was extracted from just below the sediment–water interface and at several depths from the SJ, AI-3, and LFP cores using rhizons (0.15  $\mu\text{m}$  pore size; Rhizosphere Research Products). The sediment cores from BB and SP were too loosely packed to retain enough porewater for down-core sampling. At these sites, we sampled shallow porewaters in the field by inserting a rhizon at ~2 cm below the sediment–water interface. Sediment cores were either halved or extruded for subsampling for sedimentological and geochemical analyses. All sediment and water samples were catalogued with International Geo Sample Numbers (IGSNs; [geosamples.org](http://geosamples.org)); IGSNs are listed in the appropriate supplemental tables. Sample treatment methodologies can be found in the Appendix S1.

Biological samples were collected in Fall 2017 from a dissected microbialite from LFP (Figure 1) and in Fall 2018 from sediment and microbialite samples at each of the South Arm sites (Table 1). The Fall 2017 samples were flash-frozen in liquid nitrogen in the field and then extracted using the DNeasy PowerSoil DNA isolation kit (Qiagen, Cat#1288). October 2018 samples were collected in 2-ml lysis tubes filled with Zymo Research BashingBeads and DNA preservation buffer. Cells were lysed in the field by adhering lysis tubes to a reciprocating saw for >1 min. October 2018 samples were extracted using the Zymo Research Quick-DNA Fecal/Soil Microbe DNA Miniprep Kit (Cat#D6010).

1.2 cm by 15 cm strips of 24-gauge silver (Rio Grande Co.) were polished using corundum ( $\text{Al}_2\text{O}_3$ ) powder, rinsed with acetone and deionized water, and wiped with a Kimwipe prior to transport to the field. At each site, we placed a silver strip below the sediment–water interface for at least 20 min to provide a substrate for precipitation of silver sulfide ( $\text{Ag}_2\text{S}$ ) from reduced sulfur species. Strips were removed from the sediment water interface by gloved hands, dried, and wrapped in Kimwipes, and sealed in individual sample bags. Silver strips were later imaged on a flatbed scanner at the California Institute of Technology (Caltech).

TABLE 1 Field sampling, subsampling, and analytical metadata for all cores and sites

Site	Sampling season	Latitude (°N)	Longitude (°W)	Water temperature (°C)	Depth sampled (cm)	pH	Salinity (%)	Specific gravity	Sample types	Analyses
Antelope Island causeway (AI-3)	Fall 2017	41.062044	112.23583		0	8.615			Water, sediments	$\delta^{13}\text{C}_{\text{org}}$ , $\delta^{13}\text{C}_{\text{carb}}$ , $\delta^{18}\text{O}_{\text{carb}}$ , $\Delta_{47\text{p}}$ , DI
					6	8.058				
					12					
					16					
					20					
					24					
					28					
Spring 2018		41.06201	112.23580		0	8.500			Water, sediments	$\delta^{13}\text{C}_{\text{org}}$ , $\delta^{13}\text{C}_{\text{DIC}}$ , $\delta^{13}\text{C}_{\text{carb}}$ , $\delta^{18}\text{O}_{\text{carb}}$ , DI, %TOC, [DIC]
					1	7.610				
					2	7.620				
					4					
					6	7.370				
					12	7.240				
Fall 2018		41.06218	112.23579	23	0				Sediments	
					1					
					6					
Bridger Bay (BB)	Fall 2017	41.050839	112.25688		0	8.296			Water, sediments	$\delta^{13}\text{C}_{\text{carb}}$ , $\delta^{18}\text{O}_{\text{carb}}$ , $\Delta_{47\text{p}}$ , DI
					4	7.905				
					8					
					12					
Spring 2018		41.050839	112.25688	13.5	0	8.250			Water, sediments	$\delta^{13}\text{C}_{\text{DIC}}$ , $\delta^{13}\text{C}_{\text{carb}}$ , $\delta^{18}\text{O}_{\text{carb}}$ , DI, [DIC]
					2					
Fall 2018		41.05308	112.25528	21	0				Sediments	
					1					
					4					

(Continues)

TABLE 1 (Continued)

Site	Sampling season	Latitude (°N)	Longitude (°W)	Water temperature (°C)	Depth sampled (cm)	pH	Salinity (%)	Specific gravity	Sample types	Analyses
Ladyfinger Point (LFP)	Fall 2017	41.060579	112.24882		0	7.763			Water, sediments	$\delta^{13}\text{C}_{\text{org}}$ , $\delta^{13}\text{C}_{\text{carb}}$ , $\delta^{18}\text{O}_{\text{carb}}$ , $\Delta_{47}$ DI, %TOC
					4					
					6	7.500				
					12					
Spring 2018	41.060579	112.24882		0	8.200				Water, sediments	$\delta^{13}\text{C}_{\text{org}}$ , $\delta^{13}\text{C}_{\text{DIC}}$ , $\delta^{13}\text{C}_{\text{carb}}$ , $\delta^{18}\text{O}_{\text{carb}}$ , DI, %TOC, [DIC]
					1	7.500				
					4	7.040				
Fall 2018	41.06071	112.24964	19	0					Sediments, subaerial and subaqueous microbialites	$16\text{S}$ , $\delta^{13}\text{C}_{\text{org}}$ , $\delta^{13}\text{C}_{\text{carb}}$ , $\delta^{18}\text{O}_{\text{carb}}$ , $\Delta_{47}$ %TOC
					1					
					4					
Spiral Jetty (SJ)	Spring 2018	41.43639	112.66999	0	7.200				Water, sediments	$\delta^{13}\text{C}_{\text{org}}$ , $\delta^{13}\text{C}_{\text{DIC}}$ , $\delta^{13}\text{C}_{\text{carb}}$ , $\delta^{18}\text{O}_{\text{carb}}$ , $\Delta_{47}$ DI, %TOC, [DIC]
					2					
					8					
					14	6.310				
GSL State Park (SP)	Spring 2018	40.726516	112.23016	0	8.600				Water, sediments	$16\text{S}$ , $\delta^{13}\text{C}_{\text{DIC}}$ , $\delta^{13}\text{C}_{\text{org}}$ , $\delta^{13}\text{C}_{\text{carb}}$ , $\delta^{18}\text{O}_{\text{carb}}$ , $\Delta_{47}$ DI, %TOC, [DIC]
					2					
					3					
					6					
					9					
					12					
					15					
Fall 2018	40.72847	112.23399	18	0					Sediments, microbialite, microbial mat	$16\text{S}$ , $\delta^{13}\text{C}_{\text{org}}$ , $\delta^{13}\text{C}_{\text{carb}}$ , $\delta^{18}\text{O}_{\text{carb}}$ , %TOC
					1					
					4					

Abbreviations:  $16\text{S}$ ,  $16\text{S}$  rRNA amplicon sequencing; DI, dissolved ion concentrations.

## 2.2 | Stable isotope geochemistry

All isotope ratios are reported using delta notation in parts per thousand (‰) on the VPDB scale, except for calculated  $\delta^{18}\text{O}_{\text{water}}$  compositions which are reported on the VSMOW scale. Carbon and oxygen isotope ratios were determined at the University of Colorado Earth Systems Stable Isotope Laboratory (CUBES-SIL) and at Caltech using a Thermo Delta V continuous flow isotope ratio mass spectrometer (CF-IRMS). Samples were prepared online with an elemental analyzer (EA;  $\delta^{13}\text{C}_{\text{org}}$ ) or Thermo Gasbench II ( $\delta^{13}\text{C}_{\text{carb}}$ ,  $\delta^{13}\text{C}_{\text{DIC}}$  and  $\delta^{18}\text{O}_{\text{carb}}$ ) peripheral after sample preparation steps (e.g., organic carbon removal from carbonates, and vice versa) described in the Appendix S1.  $\delta^{13}\text{C}_{\text{DIC}}$ ,  $\delta^{13}\text{C}_{\text{carb}}$ , and  $\delta^{18}\text{O}_{\text{carb}}$  values were corrected for sample size dependency and then normalized to the VPDB scale with a three-point calibration (Coplen et al., 2006) using NBS-19, Yule marble (YULE), and Harding Icelandic Spar (HIS; Table S1). The analytical precision based on replicate analyses of standard materials was 0.1‰ for both carbon and oxygen.

For organic  $\delta^{13}\text{C}$  measurements made at Caltech, sucrose and urea standards were used for correcting for sample size dependency and converting raw ratios to the VPDB scale with a two-point calibration. Pugel (Princeton University gelatin) and HOS (high organic sediment) were used for this correction at CUBES-SIL.

### 2.2.1 | Clumped isotope thermometry and water oxygen isotopes

The carbonate clumped isotope thermometer is based on the enhanced thermodynamic stability of “clumping” of the rare, heavy isotopes of carbon and oxygen ( $^{13}\text{C}$  and  $^{18}\text{O}$ ) at low temperatures (Eiler, 2007). This quantitative thermometer relies on the measurement of the mass-47 anomaly ( $\Delta_{47}$ ), which is defined as the enrichment of the  $^{13}\text{C}^{18}\text{O}^{16}\text{O}$  isotopologue of  $\text{CO}_2$  relative to a stochastic distribution of the heavy isotopes among all  $\text{CO}_2$  molecules:  $\Delta_{47} = \frac{^{47}\text{R}}{^{47}\text{R}^*} \times 1,000$ , where  $^{47}\text{R} = [^{13}\text{C}^{16}\text{O}^{18}\text{O} + ^{12}\text{C}^{17}\text{O}^{18}\text{O} + ^{13}\text{C}^{17}\text{O}_2]/[^{12}\text{C}^{16}\text{O}_2]$  and \* denotes a stochastic distribution of isotopes. The advantage of the clumped isotope thermometer over oxygen isotope-based thermometry is that the temperature estimate is independent of the bulk isotopic composition and thus requires no assumptions about  $\delta^{18}\text{O}_{\text{carb}}$  or  $\delta^{18}\text{O}_{\text{water}}$ . This means the temperature can be used to calculate  $\delta^{18}\text{O}$  of ancient waters when paired with  $\delta^{18}\text{O}_{\text{carb}}$  values of the same sample, which is measured concurrently with mass-47 measurements.

Carbonate clumped isotope measurements were made at the California Institute of Technology over three analytical sessions from May to June 2019 (Table 2). Clumped isotope measurements of carbonates were analyzed by phosphoric acid digestion in a common acid bath at 90°C to yield  $\text{CO}_2$  that could be measured by IRMS. Evolved  $\text{CO}_2$  was passed through the Caltech “Autoline,” which is an automated system of traps for purifying the gases prior to analysis. Purified  $\text{CO}_2$  was then analyzed on a ThermoScientific MAT253 gas source mass spectrometer, specifically MS 1 of Huntington et al. (2009). We measured  $\delta_{44-49}$ ,  $\delta^{13}\text{C}_{\text{CO}_2}$ , and  $\delta^{18}\text{O}_{\text{CO}_2}$

relative to an Oztech isotopic standard gas (CALT-2049C,  $\delta^{13}\text{C} = -3.62$  vs. VPDB;  $\delta^{18}\text{O} = 24.97\text{‰}$  vs. VSMOW; VSMOW used in  $\Delta_{47}$  calculations) used as the working reference gas, and computed  $\Delta_{47}$  and  $\Delta_{48}$  relative to the working gas reference frame. The  $\Delta_{47}$  values were projected from a working gas reference frame to the Carbon Dioxide Equilibrium Scale (CDES; Dennis, Affek, Passey, Schrag, & Eiler, 2011) using either standard  $\text{CO}_2$  gases heated to 1,000°C (HG) and  $\text{CO}_2$  equilibrated through reaction with water at 25°C (EG) or carbonate standards to allow for inter-laboratory comparison (details and empirical transfer functions in Appendix S1). The  $\Delta_{47,\text{CDES},90}$  values were corrected to an acid digestion temperature of 25°C ( $\Delta_{47,\text{CDES},25}$ ) using the temperature-dependent acid fractionation factor for calcite computed by Defliese, Hren, and Lohmann (2015). Samples were screened for potential contamination by identifying “ $\Delta_{48}$  excess” using a statistical regression of the  $\delta_{48} - \Delta_{48}$  HG line (see Appendix S1). We then standard corrected all the  $\Delta_{47,\text{CDES},25}$  values for each of the three sessions based on accepted values for interlaboratory carbonate standards spanning a range of formation temperatures. Individual replicates were averaged together to create final sample  $\Delta_{47}$  values, and sample-average  $\Delta_{47}$  errors were calculated in quadrature considering the “external” uncertainty of each replicate analysis

(see Appendix S1):  $\sigma_{\Delta_{47,\text{CDES},25}} = \sqrt{\frac{\sum \sigma_{\text{external}}^2}{n}}$ . Finally, temperatures

were calculated for each sample using the  $T - \Delta_{47}$  calibration of Ghosh et al. (2006) adjusted to CDES (Dennis et al., 2011). See Appendix S1 for discussion of  $T - \Delta_{47}$  calibration determination and temperature error propagation procedure.

Using  $T(\Delta_{47})$ , we calculated the oxygen isotopic composition of carbonate formation water initially assuming equilibrium oxygen isotope fractionation between carbonate and water (O’Neil et al., 1969) and that carbonates formed in equilibrium with respect to  $\Delta_{47}$ . We used  $T(\Delta_{47})$  measurements with the temperature-dependent calcium carbonate-water fractionation factor ( $\alpha_{\text{CaCO}_3-\text{H}_2\text{O}}$ ) equation of Kim and O’Neil (1997) to calculate  $\delta^{18}\text{O}_{\text{water}}$ .

## 2.3 | Dissolved ions

Parallel ion chromatography systems operating simultaneously (Dionex ICS 200, Environmental Analysis Center, Caltech) were used to measure  $\text{Ca}^{2+}$ ,  $\text{Mg}^{2+}$ ,  $\text{K}^+$ ,  $\text{Na}^+$ ,  $\text{NH}_4^+$ ,  $\text{SO}_4^{2-}$ , and  $\text{Cl}^-$ . Lake and porewater samples were diluted ~333 parts milliQ water to one part sample water before analysis (Table S2). See Appendix S1 and Table S2 for details of serial anion and cation chromatography and column chemistry, data processing in Chromeleon software, and standardization.

## 2.4 | Sedimentology and microscopy

Samples for sedimentology were not subjected to organic or inorganic C removal protocols, but were gently rinsed with DI water and

TABLE 2 Summary of clumped isotope analyses

Sample ID	Site	Depth (cm)	Season	n	$\delta^{13}\text{C}$ (‰ VPDB $\pm$ SE)	$\delta^{18}\text{O}_c$ (‰ VPDB $\pm$ SE)	$\delta_{47}$ (‰ SG-WG $\pm$ SE <sup>a</sup> )	$\Delta_{47,\text{CDES},25}$ (‰ $\pm$ SE <sup>a</sup> )	$T^*$ (°C $\pm$ SE <sup>a</sup> )
AI-3_0_O17	AI-3	0	Fall 2017	3	0.107 $\pm$ 0.005	-8.216 $\pm$ 0.011	9.394 $\pm$ 0.050	0.807 $\pm$ 0.019	6.7 $^{+3.7}_{-3.3}$
AI-3_1_O18	AI-3	1	Fall 2018	5	0.553 $\pm$ 0.006	-7.968 $\pm$ 0.012	10.197 $\pm$ 0.052	0.921 $\pm$ 0.019	-11.0 $\pm$ 2.7
AI-3_6_O18	AI-3	6	Fall 2018	4	-0.945 $\pm$ 0.007	-9.596 $\pm$ 0.013	6.896 $\pm$ 0.054	0.832 $\pm$ 0.019	2.6 $^{+3.2}_{-3.1}$
AI-3_12_O17	AI-3	12	Fall 2017	3	1.249 $\pm$ 0.006	-7.573 $\pm$ 0.012	11.195 $\pm$ 0.052	0.793 $\pm$ 0.024	9.3 $\pm$ 3.7
AI-3_28_O17	AI-3	28	Fall 2017	3	-2.752 $\pm$ 0.005	-10.876 $\pm$ 0.011	3.711 $\pm$ 0.038	0.788 $\pm$ 0.028	10.0 $\pm$ 3.2
BB0_O17	Brider Bay	0	Fall 2017	4	4.143 $\pm$ 0.005	-4.714 $\pm$ 0.013	17.152 $\pm$ 0.036	0.791 $\pm$ 0.027	9.7 $\pm$ 4.8
BB12_O17	Brider Bay	12	Fall 2017	3	4.315 $\pm$ 0.006	-4.666 $\pm$ 0.013	17.325 $\pm$ 0.042	0.764 $\pm$ 0.030	14.6 $^{+5.8}_{-5.4}$
SP0_M18	Great Salt Lake State Park	0	Spring 2018	4	4.217 $\pm$ 0.005	-4.590 $\pm$ 0.012	17.345 $\pm$ 0.027	0.774 $\pm$ 0.025	12.7 $^{+4.7}_{-4.5}$
SP15_M18	Great Salt Lake State Park	15	Spring 2018	4	4.271 $\pm$ 0.007	-4.591 $\pm$ 0.012	17.373 $\pm$ 0.041	0.776 $\pm$ 0.011	12.2 $\pm$ 2.0
LFP0_O17	Lady Finger Point	0	Fall 2017	4	3.808 $\pm$ 0.006	-4.875 $\pm$ 0.011	16.619 $\pm$ 0.041	0.786 $\pm$ 0.026	10.6 $^{+4.8}_{-4.7}$
LFP1_O18	Lady Finger Point	1	Fall 2018	1	4.634 $\pm$ 0.008	-5.001 $\pm$ 0.016	17.290 $\pm$ 0.064	0.777 $\pm$ 0.021	12.2 $^{+3.9}_{-3.8}$
LFP4_O18	Lady Finger Point	4	Fall 2018	3	4.512 $\pm$ 0.008	-4.920 $\pm$ 0.016	17.255 $\pm$ 0.067	0.777 $\pm$ 0.033	12.1 $^{+6.1}_{-5.8}$
LFP12_O17	Lady Finger Point	12	Fall 2017	5	3.799 $\pm$ 0.007	-5.013 $\pm$ 0.012	16.469 $\pm$ 0.046	0.793 $\pm$ 0.024	9.2 $^{+4.2}_{-4.1}$
SJ2_M18	Spiral Jetty	2	Spring 2018	3	4.362 $\pm$ 0.006	-4.528 $\pm$ 0.012	17.577 $\pm$ 0.038	0.788 $\pm$ 0.028	10.2 $\pm$ 5.1
SJ8_M18	Spiral Jetty	8	Spring 2018	3	3.951 $\pm$ 0.005	-5.095 $\pm$ 0.011	16.549 $\pm$ 0.037	0.780 $\pm$ 0.027	11.8 $\pm$ 4.9

Note: Temperatures are calculated using the calibration of Ghosh et al. (2006) converted from CIT to Carbon Dioxide Equilibrium Scale (CDES).

<sup>a</sup>Standard error of analytical errors of replicate measurements propagated through error of the HG correction in quadrature.

air-dried. Sediment samples from cores were analyzed for grain size and shape using a Retsch Camsizer P4 at the University of Colorado Boulder (CU). Camsizer data were used to quantify the composition of grainy samples by distinguishing the mud-size fraction (grain diameter  $<62.5\text{ }\mu\text{m}$ ), the ooid fraction (grain diameter  $>62.5\text{ }\mu\text{m}$ , roundness and sphericity  $>0.8$ ), and the remainder. One sample from each core was prepared as a polished thin section by Spectrum Petrographics via embedding loose sediment in epoxy. This thin section preparation method does not preserve spatial relationships among grains or porosity. Therefore, thin sections were used to compare grain types and fabrics among samples, while fresh sample material was used for determining facies. Thin sections were examined using plane- and cross-polarized transmitted light using a Zeiss Axio Imager M2 at CU and a Leica DM2500P at Caltech. Point counts of sediment composition of representative thin sections of grainy samples were performed using JMicrovision (401 counts/sample; Roduit, 2019) to characterize the types of non-ooid grains in these samples.

Grain mounts of microbialite intraclasts and ooids were carbon-coated and examined using a Zeiss 1550VP Field Emission Scanning Electron Microscope (FESEM) at Caltech. Chemical compositions were evaluated using an Oxford X-Max X-ray Energy Dispersive Spectrometer (EDS) with a working distance of 10.5 mm and accelerating voltage of 15 kV.

## 2.5 | Sequencing and phylogenetic analyses

DNA was amplified using the 515f/926r primer pair to amplify a segment of the V4–V5 hypervariable region, with Illumina adapters on the 5' ends (Parada, Needham, & Fuhrman, 2016; Quince, Lanzen, Davenport, & Turnbaugh, 2011). Assembled amplicon sequence variant reads (hereafter referred to as ASVs) have been deposited to GenBank®, a public genetic sequence database, under the accession KDOU00000000. The version described in this paper is the first version, KDOU01000000. Details of sequence analyses using the QIIME 2 pipeline (version 2019.4; Bolyen et al., 2018) can be found in the Appendix S1. ASVs classified as mitochondrial or chloroplast sequences were filtered from the dataset and analyzed separately. To ensure even sampling, a sequence cutoff of 1,729 was used, which retained all samples while maximizing sequence sampling depth. In order to assess beta diversity, sample distance matrices were generated using UniFrac distances and Bray–Curtis dissimilarity indices; the former metric calculates community distance by considering both the relative abundance of different organisms present in a sample as well as the phylogenetic relatedness (or lack thereof) of community members while the latter metric only considers relative organism abundance in a sample (Chang, Luan, & Sun, 2011; Faith, Minchin, & Belbin, 1987; Legendre & Legendre, 2012; Lozupone, Hamady, Kelley, & Knight, 2007; Lozupone & Knight, 2005). However, because taxonomic diversity does not necessarily equate to metabolic diversity and small changes in the archaeal sequence frequency had a large influence on UniFrac distances, only Bray–Curtis distances were used for the purposes of this paper. Community differences

were then visualized using principal coordinates analysis (PCoA) plotted using EMPeror (Vázquez-Baeza, Pirrung, Gonzalez, & Knight, 2013) in QIIME.

## 3 | RESULTS

### 3.1 | Sedimentology and facies descriptions

The primary carbonate components we found in the GSL sites studied are ooids, carbonate mud, micritic grain coatings, and microbialite carbonate. Locally remobilized microbialite intraclasts (sand-size and larger) are also a common component found in our sediment cores. Here, we discuss the primary carbonate facies of the modern, nearshore GSL sediments by analogy to traditional carbonate facies terminology used to describe lithified carbonate sediments. All sedimentology raw data and analyses are publicly available through the Open Science Framework (Ingalls, Frantz, Snell, & Trower, 2020).

#### 3.1.1 | Sites SP, SJ, and BB: ooid-dominated proto-grainstone facies

The carbonate sediments collected from SP, SJ, and BB are characterized by a grainy, mud-poor facies equivalent to a proto-grainstone (i.e., not yet cemented; Figure 2a). Site SP, on the southernmost shoreline of GSL (Figure 1), is characterized by extensive microbialite mounds elongate perpendicular to shoreline growing overtop loose ooids. BB does not have microbialites, but ooid-cemented hardgrounds are characteristic of the near-shore environment. SJ, on the northernmost shoreline (Figure 1) of the North Arm, has neither hardgrounds nor microbialite, but is the only site with halite precipitation.

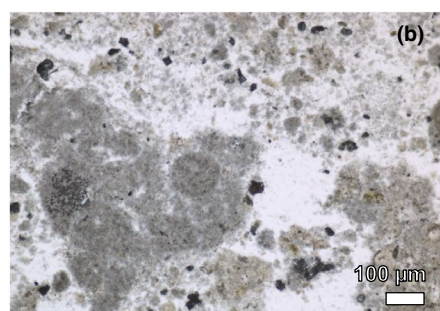
Compositionally, primarily aragonitic ooids are the dominant grain type by volume in most of these samples; however, the different macrostructures at the modern surface correlate to differences in the major non-ooid components at each site. Common accessory grain types include sand- to gravel-size microbialite intraclasts, sand-size hardground intraclasts, grapestones, broken ooid fragments, quartz proto-ooids (defined here as a quartz grain with a single, thin carbonate coating; see quartz proto-sandstone discussion), and lithic grains (Figures 2 and 3). Intraclast fabrics and sedimentary compositions correlate with the macrostructures described at the modern surface. For example, hardground intraclasts are typically composed of cemented ooids (Figure 2k), whereas microbialite intraclasts can be identified by clotted and/or mottled textures and occasional green pigments (Figure 2j). Overall compositional percentages of ooids, mud, and other sand-size grains (i.e., not ooids) were determined via Camsizer analysis; the breakdown of different types of other sand-size grains was constrained via point counts (Figure 3). These two datasets are not directly comparable due to differences in sample size ( $n_{\text{grains}} > 250,000$  for Camsizer data,  $n_{\text{grains}} = 401$  for point counts), so while the percentages listed in the following analysis correspond to constraints from Camsizer data, both datasets are visualized in Figure 3. Samples from

## Facies

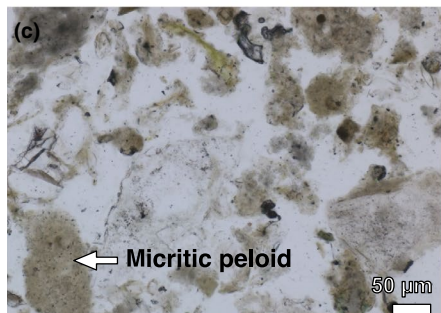
### Ooid proto-grainstone



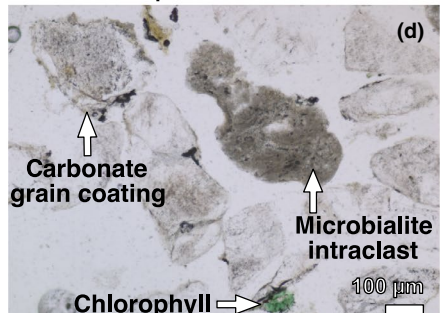
### Proto-packstone & microbialite boundstone



### Proto-wackestone



### Quartz proto-sandstone



## Carbonate grain types

### Grapestone



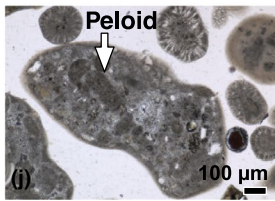
### Lithic



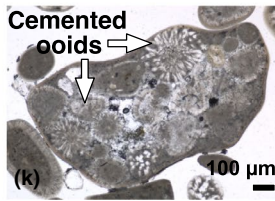
### Broken ooid



### Microbialite intraclast



### Hardground intraclast



### Proto-oid



### Peloid



BB are composed of 62% to 72% ooids, with the balance dominantly composed of broken ooids and peloids. Samples from the southernmost shoreline (SP) are composed of 72% to 78% ooids, with the balance dominantly composed of microbialite intraclasts and peloids. There is a notable change in composition at ~8 cm depth in the SJ core. SJ samples from <8 cm depth are composed of 50%–86% ooids, with the balance composed primarily of mud (14%–41%), peloids, and microbialite intraclasts. SJ samples from ≥8 cm depth are composed of only 28%–34% ooids, with the balance composed primarily of mud (~7%) and microbialite intraclasts. Both SJ samples analyzed via point counting include a minor population of lithic grains, which were not observed in samples from other locations. In general, the most

**FIGURE 2** Representative plane-polarized transmitted light images of thin sections of modern Great Salt Lake facies described in text (a–d), and the most common carbonate grain types found in cored sediments in this study (e–i). Facies images (a–d) reflect major grain types, but do not reflect original spatial relationships among grains or representative porosity due to thin section preparation methods

notable difference among ooid-dominated facies is in SJ samples from ≥8 cm depth, in which the principal compositional element, by volume, is not ooids, but instead microbialite intraclasts, making it effectively its own sub-facies. Thus, we interpret the geochemistry of SJ >8 cm depth samples separately from BB, SP, and SJ <8 cm.

### 3.1.2 | Site LFP: microbialite intraclast proto-packstone and microbialite boundstone

Ladyfinger Point lies to the north of BB, separated by a finger of Antelope Island, differentiating it from the proto-grainstone sites

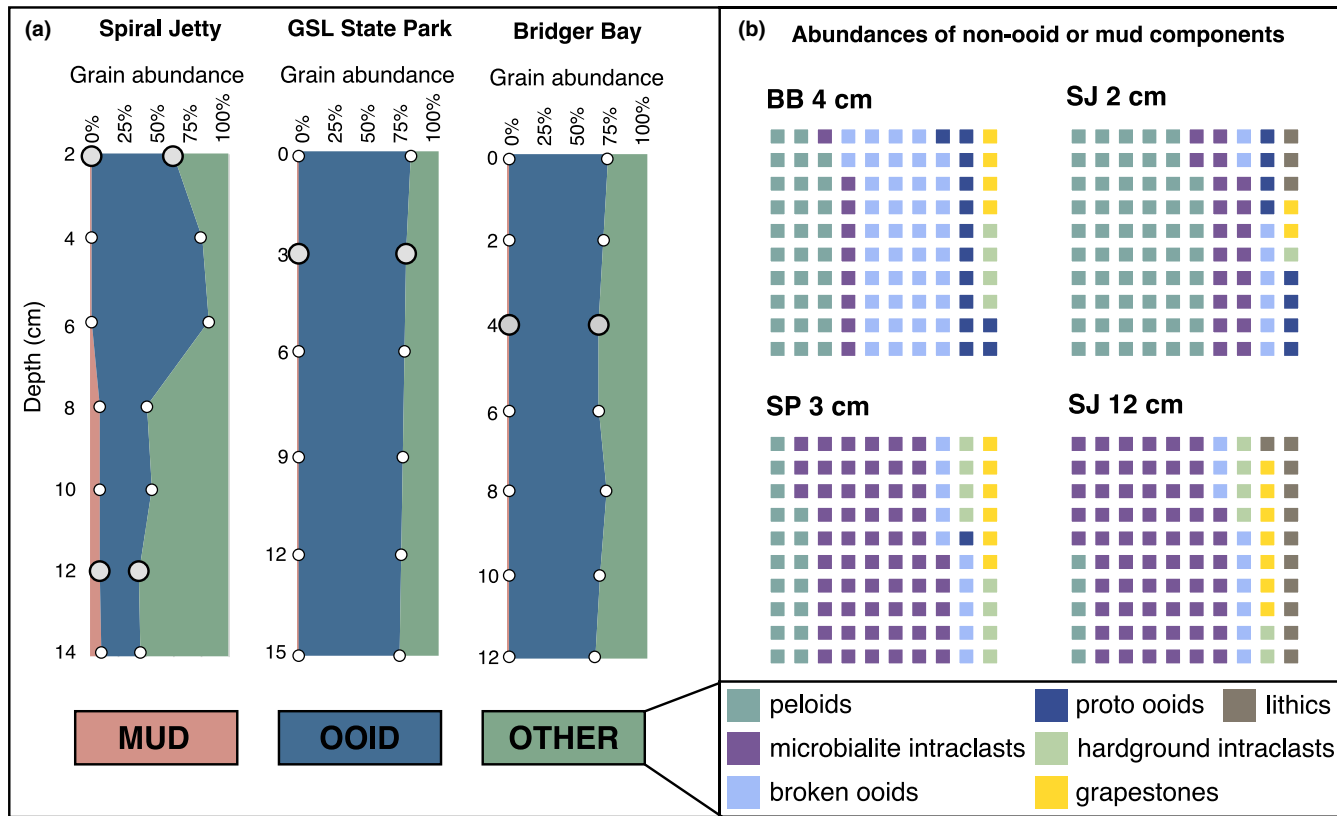


**FIGURE 3** (a) Grain type abundances in cores from the three ooid-dominated sites determined by Camsizer analyses. Larger gray circles denote the depths point-counted for quantifying “other” in (b). (b) “Other” grain types are further categorized by point counting using JMicrowision

both sedimentologically and geochemically. Seasonally subaerial/subaqueous microbialite mounds are abundant at LFP for at least tens of meters from the shoreline lakeward. Loose sediments are primarily sand-sized, remobilized microbialite intraclasts and carbonate mud (Figure 2b). A carbonate hardground horizon was struck at 4 cm depth in one of three LFP cores (Figure 1), suggesting local hardground formation in the subsurface. Authigenic magnesium silicates are also found at 4 cm depth via electron microscopy (Figure S1) and are spatially associated with microbialite intraclasts and degraded coccoid cells (potentially cyanobacteria).

### 3.1.3 | Site AI-3: organic-rich proto-wackestone and quartz proto-sandstone

Site AI-3 is a muddy bay on the northern end of Antelope Island constrained on the east by the Antelope Island causeway. The organic-rich mud at AI-3 is interfingered with sand eroded off of the causeway, delivering an anthropogenic sediment source to this site. The three cores from AI-3 were collected from the interface of the anthropogenic sand and organic-rich mud, and thus, there are both spatial and temporal variability in sediment composition at this site. During lake level high, the Spring 2018 core was collected closer to the causeway and thus has a higher fraction of anthropogenic quartz

sand and other lithics. The Fall cores were collected during lake level low, and thus, we were able to collect cores that better represent the organic sedimentation and carbonate production of the bay. All AI-3 cores had higher organic matter content than the oolitic sites, but Fall 2017 and 2018 cores were more organic-rich than the Spring 2018 core, for these spatial reasons. Microbialite intraclasts were identified in thin sections from AI-3 cores from Fall 2017 and Spring 2018 (Figure 2c,d). Here, we describe the two distinct sediment compositions by their likely eventual lithified carbonate rock types.

#### Organic-rich proto-wackestone

The Fall 2017 and 2018 cores were dominantly muddy, with much higher fractions of organic matter than the Spring 2018 core (Figure 2c). Silt to fine sand size quartz occurs, but in lesser abundance than the Spring 2018 core (proto-sandstone facies). Nearly, all carbonate in this facies can be characterized as micritic peloids and microbialite intraclasts (Figure 2i,j). A putrid aroma was notable at site AI-3 during both Fall coring time points.

#### Quartz proto-sandstone

The Spring 2018 core was collected slightly closer to the causeway due to a higher lake elevation and therefore subject to a greater flux of anthropogenically deposited sand. The Spring 2018 core was dominantly composed of quartz sand with thin, bladed, and micritic

ragonite; we define this specific type of grain coating as “proto-oid” (Figure 2h). Green pigments that we interpret as chlorophyll are associated with some of the aragonite laminae, suggesting a potential association between the carbonate coatings and photosynthetic microbes (Figure 2d).

### 3.1.4 | Microbialite boundstone

Mounded microbial mats were observed on the crests of ripple-laminated ooid sands in the shallow water of LFP and SP (Figure 1d,f,h). The mounds typically have ~10 to 20 cm of relief from the modern sediment–water interface. The domal structures are primarily cemented ooid mounds topped with microbial mats at SP (Figure 1j), and microbially bound sand-sized carbonate grains at LFP (Figure 1h,i). At both sites, the tops of mounds are covered and connected to neighboring mounds by microbial biofilms and a 0.1- to 1 cm-thick, bumpy layer of brine fly casings. The most exterior carbonate layer is primarily white with some areas of pink or green presumably associated with the photosynthetic biological community, and easily broken. The interior of the mounds at both sites is loose to partially cemented, light to dark gray, carbonate mud, and sand-size carbonate clasts and ooids, and produces a sulfidic smell when broken open. The interior and exterior ooid grains are a mixture of oblong ooids that are commonly carbonate-coated brine shrimp pellets and ooids with lithic nuclei.

## 3.2 | Water chemistry

### 3.2.1 | Dissolved ions and carbonate saturation

The primary cation and anion concentrations used in carbonate saturation calculations ( $Mg^{2+}$  and  $Ca^{2+}$ ) or relevant products and reactants of metabolisms discussed in this work are provided here. A full suite of cation and anion concentration data for all sites and multiple seasons can be found in the Appendix S1 (Figure S2; Table S2). Overall, cation and anion concentrations were consistently higher in the North Arm (SJ) than any site in the South Arm (Figure S2; Table S2).

Sulfate ranged from 1.1 to 118.5 mM ( $\pm 1.9\%$ ) in the South Arm, with the highest concentrations at BB, and lowest concentrations at depth in the LFP and AI-3 cores, particularly at the base of AI-3. We qualitatively observed detectable amounts of thiosulfate in cores from AI-3. Sulfate concentrations increased with depth in the North Arm (SJ) from 266.1 to 650.1 mM.

Of the major carbonate-binding cations, magnesium concentrations were two orders of magnitude greater than calcium.  $[Mg^{2+}]$  ranged from 121.3 to 229.9 mM ( $\pm 0.6\%$ ) in the South Arm and 508.7 to 618.6 mM in the North Arm.  $[Mg^{2+}]$  was generally lower in the lakewater than the porewater and variable at depth.  $[Ca^{2+}]$  ranged from 2.7 to 8.7 mM ( $\pm 7.7\%$ ) in the North and South Arms, with no consistent trend with depth.

### 3.2.2 | Carbonate speciation and carbonate mineral saturation

Dissolved inorganic carbon concentrations (Table S4), ion concentrations (Table S2), and pH measurements (Table 1) were used to calculate the carbonate saturation state with respect to aragonite ( $CaCO_3$ ) using PHREEQC with the PITZER database (Parkhurst & Appelo, 2013). In Spring 2018, lakewater  $\Omega_{arag}$  ranged from 1.91 to 2.29 in the South Arm and 0.63 in the North Arm.  $\Omega_{arag}$  ranged from 0.10 to 3.98 in sediment porewaters across all sites (Figure 4). Lakewater pH was 7.2 in the North Arm and ranged from 8.2 to 8.6 in the South Arm in Spring 2018 (Table 1; Figure 4). Porewater pH was always lower than lakewater, ranging from 6.3 to 8.1 (Table 1).

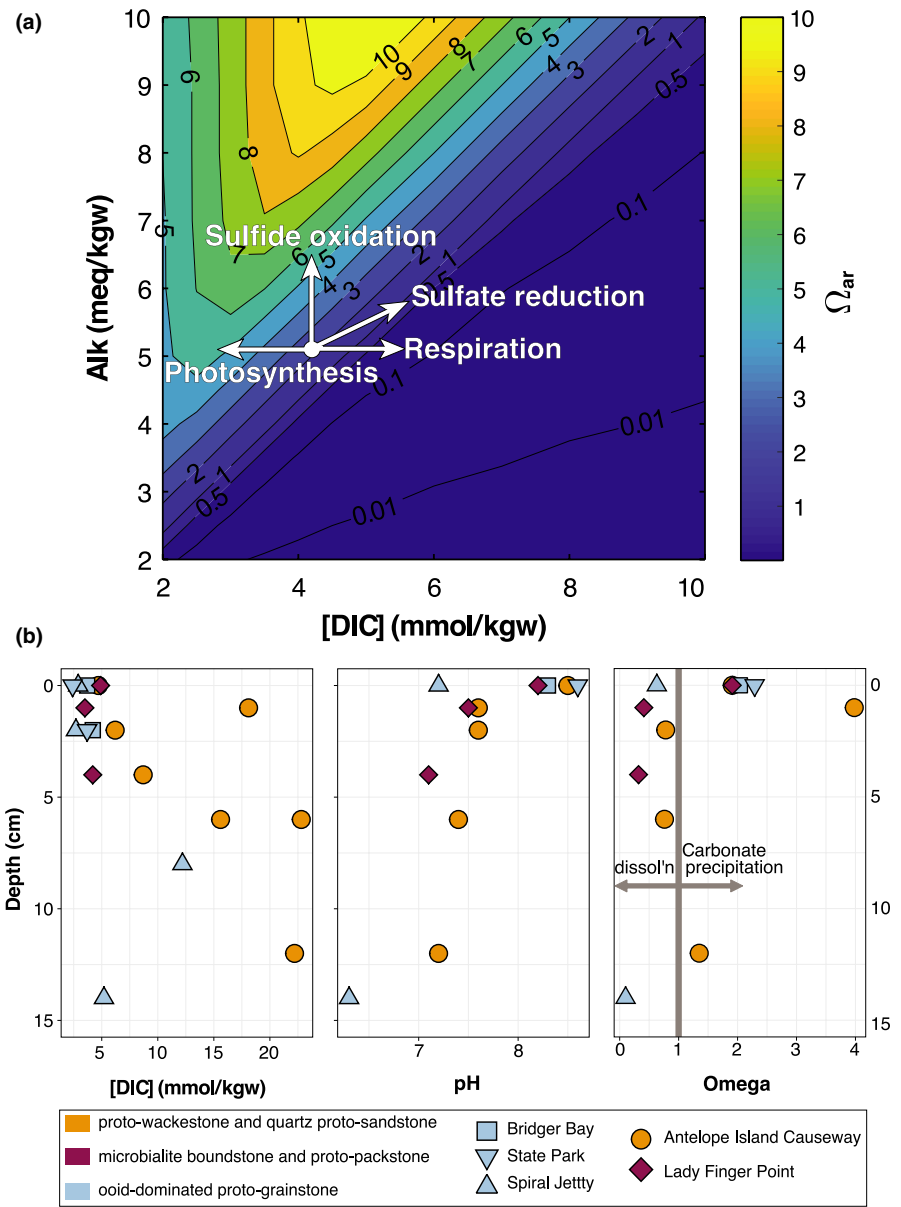
## 3.3 | Carbonate carbon and oxygen isotopes

All stable isotope raw data and processing scripts are publicly available through the Open Science Framework (Ingalls et al., 2020).  $\delta^{18}O_{carb}$  and  $\delta^{13}C_{carb}$  from the sediment cores varied by  $6.9\%$  and  $11.8\%$  versus VPDB, respectively, between all coring sites and depths (Figures 5 and 6).  $\delta^{18}O_{carb}$  and  $\delta^{13}C_{carb}$  of AI-3 ranged from  $-10.7\%$  to  $-7.1\%$  and  $-1.7\%$  to  $3.2\%$ , respectively.  $\delta^{18}O_{carb}$  and  $\delta^{13}C_{carb}$  of ooid sites BB, SJ, and SP were more tightly clustered with a total range of  $-5.7\%$  to  $-4.1\%$  and  $1.4\%$  to  $4.6\%$ , respectively. LFP core sediments and microbialite carbonate ranged from  $-5.2\%$  to  $-3.8\%$  and  $1.3\%$  to  $10.1\%$ , respectively. The larger “error” bars associated with some measurements in Figure 6 are likely due to isotopic spatial heterogeneity within individual core depths. For example, an individual carbonate digestion for isotopic analysis could include two or three carbonate grain types, and thus, the measured composition is a weighted average of the carbonate components digested. We interpret the variability in  $\delta^{13}C_{carb}$  and  $\delta^{18}O_{carb}$  replicate measurements from the same depth to be differences between isotopic values of different carbonate grain types (Figure 3). A similar pattern was seen in replicate measurements of organic matter in AI-3.

## 3.4 | Organic carbon isotopes

$\delta^{13}C$  of bulk organic matter ranged from  $-21.3\%$  to  $-16.7\%$  in all cores (Figure 5 and Figure S3; Table S3), with the lowest values from microbialite mounds and intraclasts at LFP. There was some amount of seasonality in  $\delta^{13}C_{org}$  in the sites that were measured over multiple seasons. For example, at AI-3,  $\delta^{13}C_{org}$  increased with depth in the Spring 2018 core but decreased with depth in the Fall 2017 core.  $\delta^{13}C_{org}$  was consistently  $>2\%$  offset between Spring and Fall 2018 SP core measurements. There was no statistical correlation between  $\delta^{13}C$  of organic matter and carbonate in any of the five cores (Figure S3), a metric recently proposed for detection of meteoric alteration of sedimentary organic matter (Oehlert et al., 2012; Oehlert & Swart, 2014).

**FIGURE 4** (a) Fan diagram depicting changes in total alkalinity and dissolved inorganic carbon concentration as a result of biological activity. Contours and colors depict  $\Omega_{\text{arag}}$ .  $\Delta[\text{ALK}]/\Delta[\text{DIC}] > 1$  required for an increase in  $\Omega_{\text{arag}}$ . The white circle is Bridger Bay lake water. (b) Characteristics of carbonate chemistry ( $[\text{DIC}]$ , pH, and  $\Omega_{\text{arag}}$ ) by depth. Orange, maroon, and blue differentiate the three facies described in text and depicted in Figure 2. Site locations are marked by symbol shape



### 3.5 | Dissolved inorganic carbon isotopes

$\delta^{13}\text{C}_{\text{DIC}}$  of the lakewater at BB, SP, LFP, AI-3, and SJ were  $-0.7\text{\textperthousand}$ ,  $-0.5\text{\textperthousand}$ ,  $-2.1\text{\textperthousand}$ ,  $-2.0\text{\textperthousand}$ , and  $+4.6\text{\textperthousand}$ , respectively. The total range of  $\delta^{13}\text{C}_{\text{DIC}}$  across the five sites and all core depths was  $-5.9\text{\textperthousand}$  to  $+4.6\text{\textperthousand}$  (Table S4; Figure 5).

### 3.6 | Carbonate clumped isotope thermometry and $\delta^{18}\text{O}_{\text{water}}$ calculations

$\Delta_{47,\text{CDES},25}$  values for ooid and microbialite sites LFP, BB, SP, and SJ ranged from  $0.764 \pm 0.030$  to  $0.793 \pm 0.024\text{\textperthousand}$ , corresponding to temperatures of  $14.6^{+5.8/-5.4}\text{^\circ C}$  to  $9.2^{+4.2/-4.1}\text{^\circ C}$  (Figure 7; Table 2; Tables S5–S7). Detrital and authigenic carbonate from AI-3 yielded one  $\Delta_{47,\text{CDES},25}$  value of  $0.788 \pm 0.028$  in agreement with

the range of other samples and sites, and another  $\Delta_{47,\text{CDES},25}$  value of  $0.921 \pm 0.019\text{\textperthousand}$ . These values represent equilibrium temperatures of  $10.0 \pm 3.2$  to  $-11.0 \pm 2.7\text{^\circ C}$ , although the latter is likely the product of carbonate precipitation out of equilibrium with respect to  $\Delta_{47}$ . Calculated  $\delta^{18}\text{O}_{\text{water}}$  ranged from  $-6.2 \pm 1.0\text{\textperthousand}$  to  $-4.5 \pm 0.8\text{\textperthousand}$  VSMOW at LFP and the ooid-dominated sites, and  $-13.8 \pm 1.0\text{\textperthousand}$  to  $-10.0 \pm 1.1\text{\textperthousand}$  at AI-3 (Figure 7).

### 3.7 | Sulfide precipitation on silver strips

In the absence of sulfide minerals, microbial sulfate reduction can be detected by the precipitation of  $\text{Ag}_2\text{S}$  following the reaction of dissolved  $\text{H}_2\text{S}$  with polished silver strips. Notable  $\text{Ag}_2\text{S}$  deposits accumulated below 6–7 cm depth at AI-3 and between 0 and 10 cm depth at LFP, with hot spots of maximum precipitation at 12–14

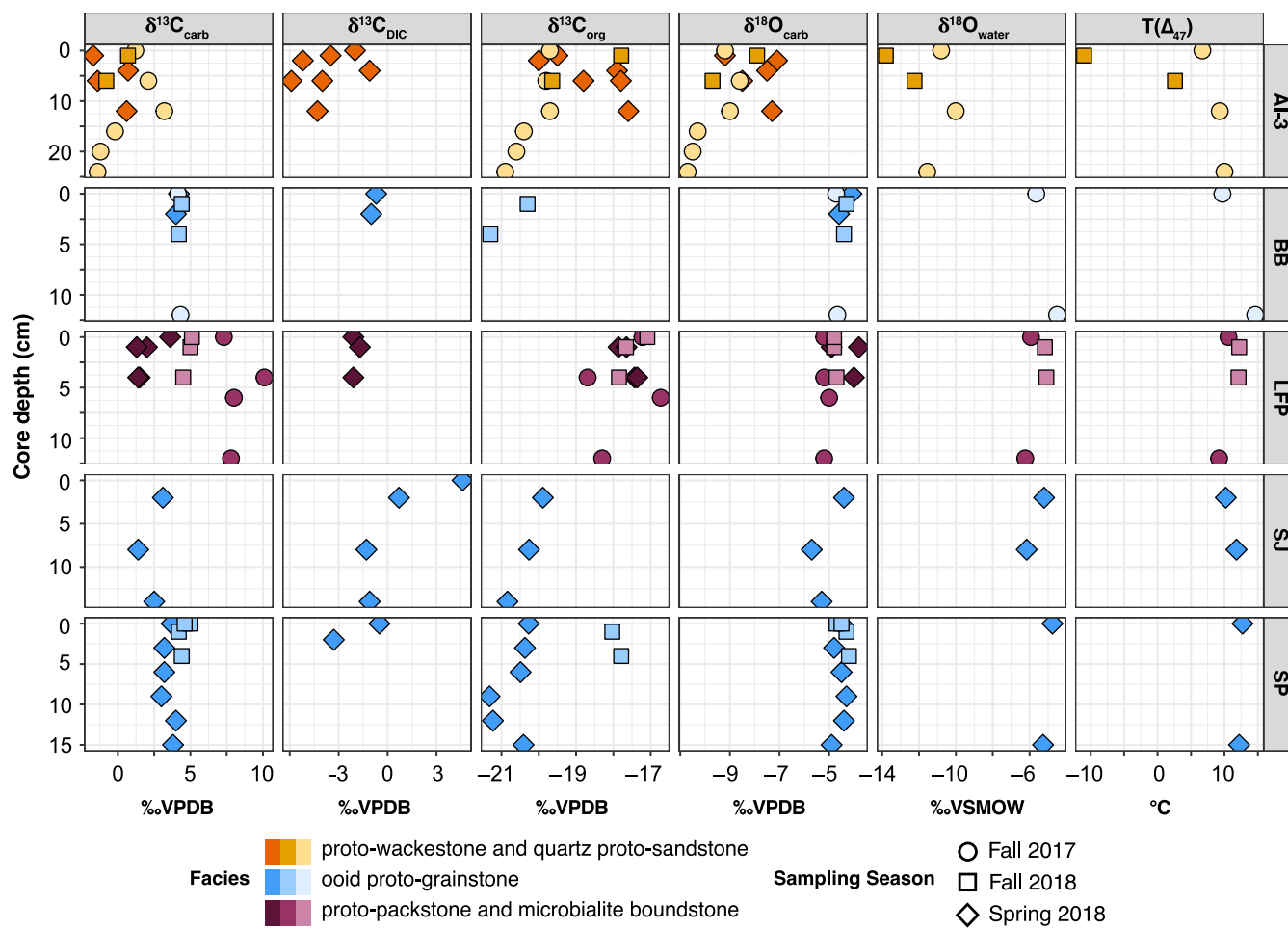


**FIGURE 5** Carbonate, dissolved inorganic carbon, and carbonate  $\delta^{13}\text{C}$ , carbonate  $\delta^{18}\text{O}$ , water  $\delta^{18}\text{O}$ , and carbonate clumped isotope temperatures from five coring sites on Great Salt Lake. As in Figure 4, facies are denoted by color, with each sampling season depicted as a shade of the same hue

and 3–5 cm, respectively. A minimal amount of  $\text{Ag}_2\text{S}$  precipitated at 13–14 cm depth at SP, and no noticeable  $\text{Ag}_2\text{S}$  formed at SJ and BB (Figure S4).

### 3.8 | Microbial community

#### 3.8.1 | Alpha diversity

All samples analyzed were well-sampled at the 1,739 sequence cut-off (Figure S5). At this sampling depth, samples contained between 202 and 397 unique ASVs. While there were significant differences in diversity between samples, no significant differences based on sample metadata (Table S8) were found except that for most of the sediment samples, surface samples were more taxonomically diverse than deep samples (Figure S6).

Notable patterns in community composition were apparent when taxonomic information was assigned to abundant ASVs. Bacteria made up 89% of all sequences while Archaea made up the remaining 11%. Of archaeal sequences, those grouping with *Thermoplasmata*

were most abundant (Figure 8). Of bacterial sequences, ASVs grouping with sulfur reducers, halophiles, and fermenters were among the most commonly identified taxa. Cyanobacteria were also abundantly represented, predominantly by the coccoidal cyanobacterium *Dactylococcopsis salina* PCC-8305. Cyanobacteria were most abundant in the October 2017 LFP microbialite exterior samples (EG, EP), but also had significant representation in 2018 sediment and microbialite samples from both LFP and SP (Figure 8). Microbialite interior samples, in contrast, had fewer Cyanobacteria and expanded representation of sulfur reducers. Sediment samples from SP had similar communities at all core depths sampled. LFP sediment samples had greater variability in surface versus deep samples, with abundant archaea in the 4-cm-depth samples (Figure 9). AI-3 samples also had large differences between the top and deep sample (Figure 9) with the 6cm samples dominated by *Halanaerobium* (Figure 8). BB sediment samples were distinct from sediments at other sites, containing a high percentage of sequences grouping with *Chloroflexi* and *Deinococcus-Thermus*, which are more typically (though not exclusively) associated with hydrothermal systems and hot springs (e.g., Bowen De León, Gerlach, Peyton, & Fields, 2013).

**FIGURE 6** Hypothesis that correlation or non-correlation between carbonate carbon and oxygen isotopes can be used to distinguish (a) climatic and hydrological versus biological controls on  $\delta^{13}\text{C}_{\text{carb}}$  in lake sediments. (b) Carbonate from all cores in this study are plotted by site location (shape) and carbonate facies (color scheme by facies as in earlier figures). Ooid, beach rock, and microbialite data from Newell et al. (2017) are plotted in gray. (c) Linear regressions of  $\delta^{13}\text{C}_{\text{carb}}$  versus  $\delta^{18}\text{O}_{\text{carb}}$  for the three facies are plotted with 95% confidence interval envelopes. Plots in (c) have the same x:y aspect ratios

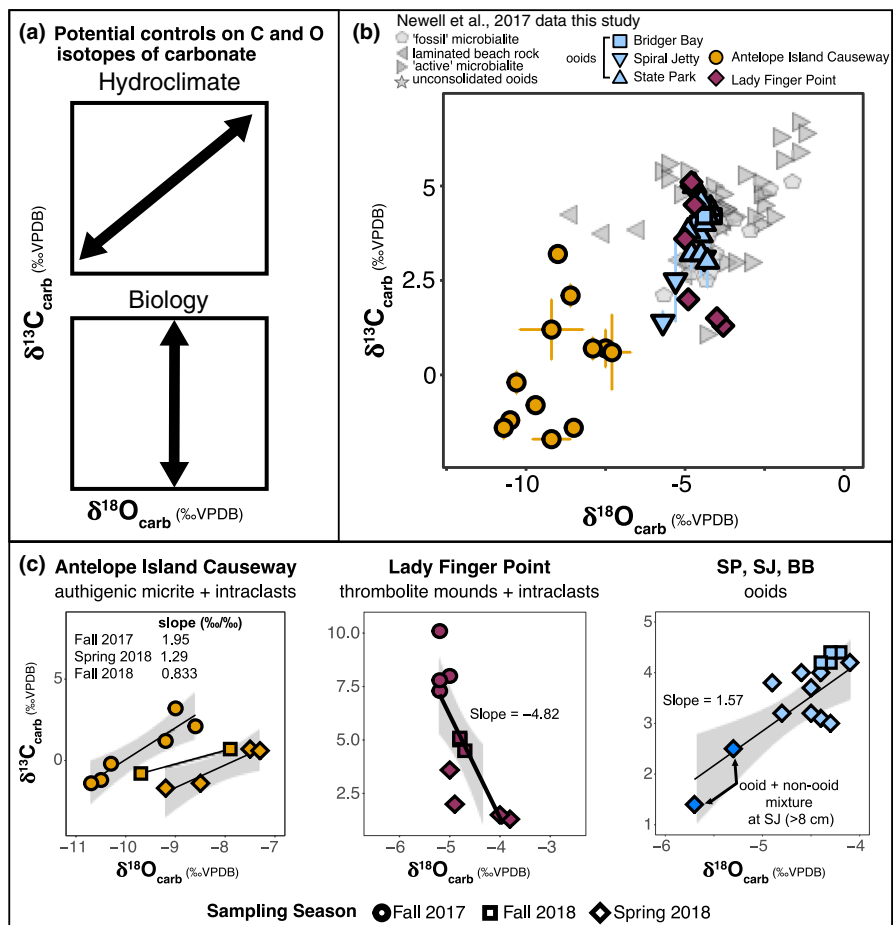
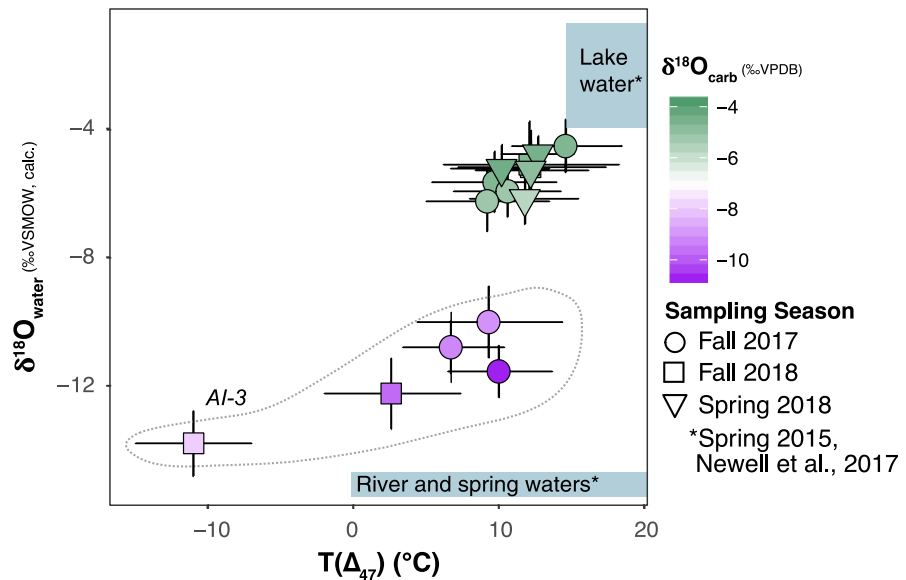


**FIGURE 7** Carbonate formation water  $\delta^{18}\text{O}$  calculated from  $\delta^{18}\text{O}_{\text{carb}}$  (color fill) and  $T(\Delta_{47})$ .  $\delta^{18}\text{O}_{\text{water}}$  of lake water and river and spring inputs, taken from Newell et al. (2017), are marked (blue) as reference to relative contribution of the two end member water sources to carbonate formation at AI-3 versus the other sites



### 3.8.2 | Beta diversity

The weighted UniFrac metric (which weights phylogenetic diversity) identified the LFP 4-cm samples as being most different from other samples as the result of a larger proportion of several groups

of Archaea (Figure S7). The Bray–Curtis metric (which does not consider phylogenetic diversity; Figure 9) highlighted the uniqueness of the 2017 LFP microbialite exterior samples (abundant cyanobacterial sequences), the AI-3 6-cm samples (abundant *Halanaerobium*), the BB samples (*Anaerolineaceae* and *Truepera*), and the group containing

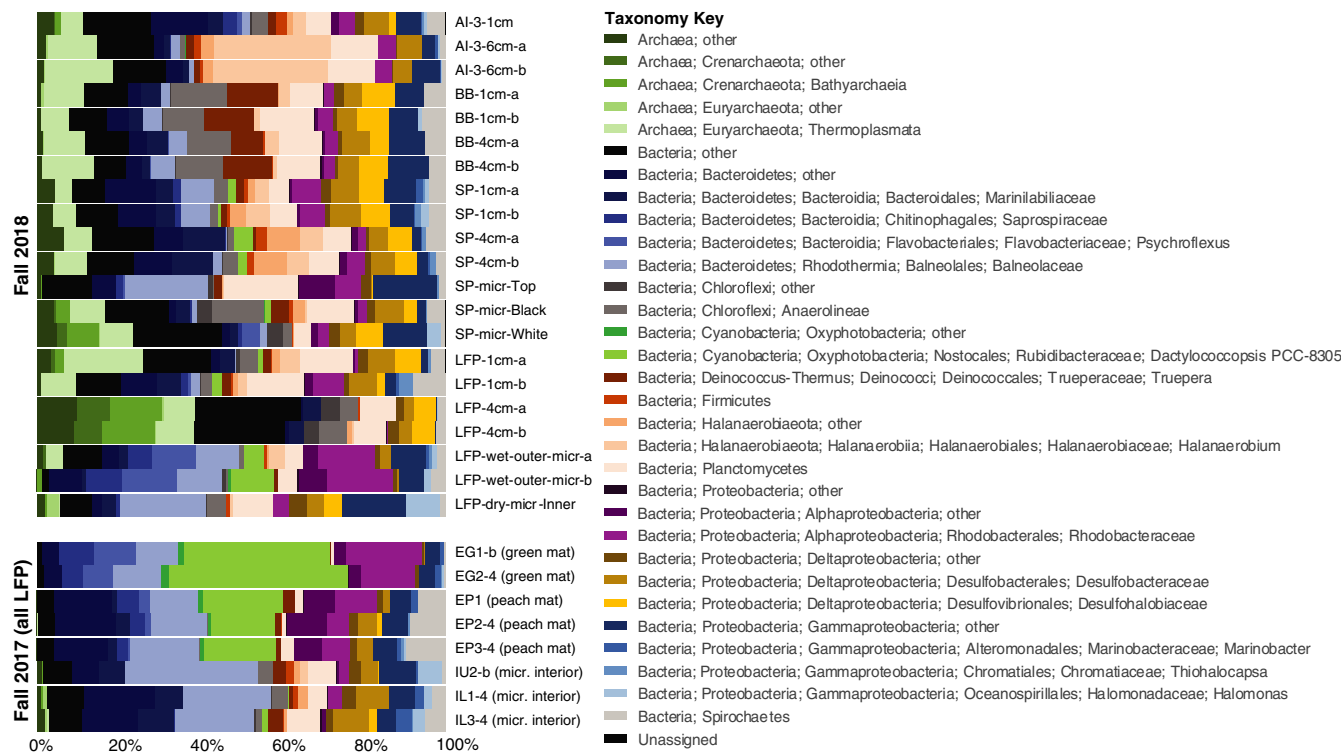


**FIGURE 8** Relative abundance of taxonomic groupings determined for each 16S amplicon sample. All Fall 2017 samples are from microbialites at LFP. Site and sample metadata can be found in Table S8

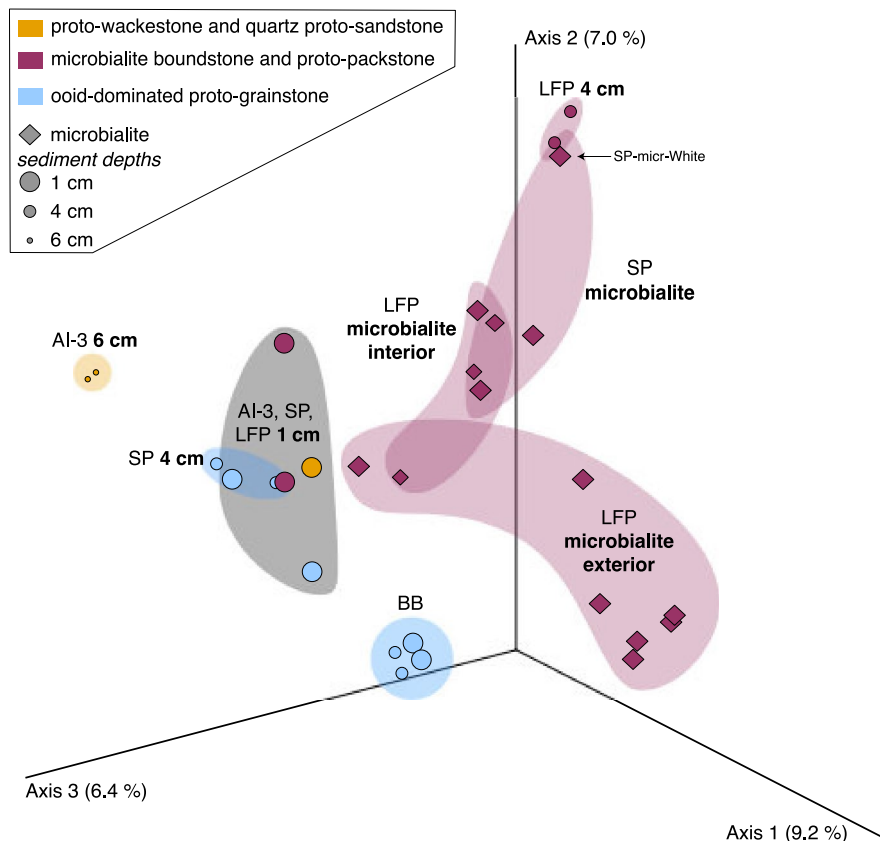


**FIGURE 9** Principal component analysis (PCoA) plot of Bray–Curtis sample distances. PCoA performs an eigen analysis on community distance data in order to permit visualization of differences in multidimensional space, where a greater distance measures greater dissimilarity. The axes have no physical meaning; rather, they represent a factor by which samples can be statistically differentiated. Envelopes group samples by sample type (sediment depth [circles] versus microbialite [diamonds]), and are colored based on facies correlation unless multiple facies types plot within a grouping (gray)

the LFP 4cm samples and the SP-micr-White sample (with abundant Archaea, especially Bathyarchaeia and other Crenarchaeia, and lower proportions of *Halanaerobium*). With few exceptions, notably LFP-wet-outer-micr, replicate samples grouped together, and shallow versus deep samples from the same site formed distinct groups (excepting BB samples).

## 4 | DISCUSSION

### 4.1 | Which carbonate facies are isotopically sensitive to microbiology and hydroclimate?

While each of the study sites have interesting microbial community and porewater chemistry compositions, the relative sensitivity to local biological processes and changes in lakewater composition varies between carbonate facies. Here, we review the evidence for sensitivity and insensitivity to local and regional processes at each of our sites to better understand how to leverage facies-specific isotope records to create more complete biogeochemical and climatic reconstructions of ancient systems.

#### 4.1.1 | Ooid-dominated proto-grainstone facies

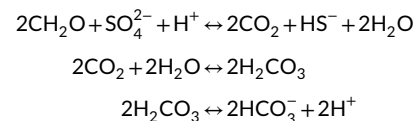
Ooids concentrically grew over a ~6,000-year interval in GSL, with the oldest inorganic  $^{14}\text{C}$  ages being ~6,600 years BP (Paradis et al., 2017). In theory, each carbonate lamina records the carbonate chemistry of the growth water at the time of precipitation. As such, bulk measurements of GSL ooids should record the integrated history of lakewater carbonate chemistry and isotopic composition over the entire duration of ooid growth, although individual ooids likely experience substantial periods of non-precipitation and/or net abrasion (Trower, Lamb, & Fischer, 2017).

The  $\delta^{18}\text{O}_{\text{carb}}$  and  $\delta^{13}\text{C}_{\text{carb}}$  values of the ooid-dominated proto-grainstone facies are comparable to microbialites, tufa, and ooid stable isotope values from Newell et al. (2017) that also record climate signals of the Pleistocene to Holocene (Figure 6b). The  $\delta^{18}\text{O}_{\text{carb}}$ – $\delta^{13}\text{C}_{\text{carb}}$  composition space of all samples measured from the proto-grainstone facies is quite limited, ranging 1.6‰ in  $\delta^{18}\text{O}_{\text{carb}}$  and 3‰ in  $\delta^{13}\text{C}_{\text{carb}}$ . However, these ranges include the two deepest samples from the Spiral Jetty core which are a mixture of ooids and non-ooid, sand-sized carbonate grains (Figure 3). The non-ooid components did not necessarily form over the same interval and record the same lake water chemistry as the ooid grains; thus, the isotopic compositions from these two samples could be more representative of a specific interval of GSL water level or chemistry, or a biological process by which ooids are seemingly unaffected. Thus, the lower  $\delta^{13}\text{C}_{\text{carb}}$  and  $\delta^{18}\text{O}_{\text{carb}}$  values of the non-ooid components could have driven the bulk sample values away from the median GSL ooid population represented by BB, SP, and upper SJ (Figure 6). If we remove these two samples from the current consideration,  $\delta^{18}\text{O}_{\text{carb}}$  and  $\delta^{13}\text{C}_{\text{carb}}$  of the ooid population

only vary by 0.8‰ and 1.4‰ (Figure 6c), respectively. Further, when the non-ooid samples are removed, there is no longer the correlation between  $\delta^{18}\text{O}_{\text{carb}}$  and  $\delta^{13}\text{C}_{\text{carb}}$  (Figure 6c) expected for carbonate sediments recording changing lake water chemistry in a closed basin (Figure 6a). We interpret the small range of these data as evidence that ooids are buffered from local and regional short-term changes to climate and hydrology by their time-averaged nature.

Further, ooid carbonate is seemingly resistant to syngenetic and early diagenetic isotopic alteration driven by microbial activity and porewater chemistry because there is little to no net carbonate production. For example, the lakewater chemistry and microbial community of SJ (Lindsay et al., 2017) are markedly different than the other sites, which are all in the South Arm. The dissolved ion compositions of both lakewater and porewater are much higher at Spiral Jetty than any of the other sites (Figure S2), with salinities twice as high. Further,  $\delta^{13}\text{C}_{\text{DIC}}$  is significantly higher in the upper sediments and lakewater at SJ than at other sites (Figure 5). However, this major discrepancy in carbon composition is currently not translated to the carbonate mineral record;  $\delta^{13}\text{C}_{\text{carb}}$  of all of the ooid sites are indistinguishable (Figure 5). In fact, the aragonite saturation states calculated for SJ lakewater and porewater are both strongly undersaturated ( $\Omega_{\text{SJ lw}} = 0.63$ ,  $\Omega_{\text{SJ pw}} = 0.1$ ), indicating that carbonate dissolution is currently favored, and thus, mediation of  $\delta^{13}\text{C}_{\text{DIC}}$  by microbes is not translated to the carbonate record due to lack of modern precipitation. Further, it is possible that the timescale since causeway construction in 1959 has been too short for the unique chemistry and microbiology that have developed in the North Arm to have affected the time-averaged carbonate mineral record contained in bulk ooid carbonate.

Along these lines, the syngenetic isotopic effects of microbial metabolisms on the DIC system will only be recorded by carbonate if there is net carbonate growth due to  $\Omega_{\text{arag}} > 1$ . Here, we consider the role of sulfur cycling metabolisms in mediating  $\Omega_{\text{arag}}$  and the isotopic signatures of modern sediments. Microbial sulfate reduction (MSR) has been linked to carbonate precipitation via organic carbon mineralization in marine and lacustrine sediments (e.g., Baas-Becking, 1934; Visscher, Reid, & Bebout, 2000), particularly within microbial mats (Buczynski & Chafetz, 1991; Jorgensen & Cohen, 1977; Lyons, Long, Hines, Gaudette, & Armstrong, 1984). Sulfate reducing bacteria (SRB) are known to use the low molecular weight organic carbon fraction of extracellular organic matter as electron donors (Decho, Visscher, & Reid, 2005), which produces DIC and sites for carbonate nucleation on the EPS matrix (Dupraz et al., 2013; Lippmann, 1973). SRB oxidize organic compounds (here, simplified bulk organic matter,  $\text{CH}_2\text{O}$ ) to reduce sulfates to sulfides:



However, to increase  $\Omega_{\text{arag}}$ , the change in [ALK] relative to the change in [DIC] must be greater than one ( $\Delta[\text{ALK}]/\Delta[\text{DIC}] > 1$ ). In the above set of reactions,  $\Delta[\text{ALK}]/\Delta[\text{DIC}] = \frac{1}{2}$ , and therefore,  $\Omega_{\text{arag}}$  decreases by sulfate reduction (Figure 4). Thus, removal of the sulfide species, either by oxidation to sulfate, reduction to elemental sulfur, or mineralization, and the resultant increase in pH and DIC is required to induce carbonate precipitation after MSR (Hammes & Verstraete, 2002; Wright, 1999). 16S rRNA data indicated that SRB are present in SP and BB sediments, but the lack of  $\text{Ag}_2\text{S}$  precipitation during the silver strip incubations at these sites suggests minimal activity by the SRB, and therefore, the net activity of SRB may have a limited impact on net carbonate precipitation-dissolution. Despite their presence, sulfate reduction could be limited due to low amounts of total organic carbon (Table S3) available as an electron donor in the ooid-dominated proto-grainstone sites. Alternatively, sulfur oxidizers could be oxidizing sulfide at a near equal amount as sulfide is being produced by MSR in the proto-grainstone facies. Sulfur oxidation increases [ALK] without any change to [DIC], thereby increasing  $\Omega_{\text{arag}}$ . This seems particularly likely in the South Arm where  $\Omega_{\text{arag}} > 1$  at the sediment-water interface at all sites. Sulfur oxidizing bacteria are present in the 16S data, including purple sulfur bacteria (Chromatiaceae, especially *Thiohalocapsa*; Figure 8); however, they do not make up a large portion of ASVs in any samples. Regardless of activity level of sulfur cyclers, the agreement in bulk isotopic composition of all ooids measured in this study and Newell et al. (2017) demonstrates that the isotopic compositions of ooids are buffered from any potential local and short-lived, biologically driven perturbations to the water and DIC isotope compositions due to their time-averaged nature.

#### 4.1.2 | Authigenic aragonite north of the Antelope Island causeway: quartz proto-sandstone facies

The thin, micritic grain coatings at AI-3 cover sand and other lithics (Figure 2d) deposited since the construction of the Antelope Island causeway. As such, the isotopic compositions of these recent grain coatings record a much shorter duration of time than ooids found at other sites and thus a less integrated solution chemistry. For example, nearly all  $\delta^{18}\text{O}_{\text{carb}}$  and  $\delta^{13}\text{C}_{\text{carb}}$  values are lower than any of the other four sites at all depths (Figure 6b), suggesting precipitation in equilibrium with lake chemistry distinct from the time at which carbonate formed at the other sites. In this section, we discuss the sensitivity of carbonate chemistry and composition of the thin carbonate grain coatings that form at AI-3 to the dynamic hydrology and heterogeneous microbial communities of this site.

At AI-3, positive  $\delta^{13}\text{C}_{\text{carb}}-\delta^{18}\text{O}_{\text{carb}}$  correlations are found in both the proto-wackestone and proto-sandstone facies (Figure 6c). From Fall 2017 to Fall 2018, the  $\delta^{13}\text{C}_{\text{carb}}/\delta^{18}\text{O}_{\text{carb}}$  slope decreases from 1.95 to 0.83. This changing relationship could reflect relative contribution of hydroclimate (greater change in  $\delta^{18}\text{O}_{\text{water}}$ , and in turn,  $\delta^{18}\text{O}_{\text{carb}}$ ) versus biological mediation of carbonate chemistry (greater

change in  $\delta^{13}\text{C}$ ) within the microenvironments sampled between core sites or seasonally. We favor the interpretation that isotopic differences between AI-3 cores is driven by heterogeneity of sedimentary composition (Figure 2c,d) and microbial communities within subsurface microenvironments at this site (Figure 9, Figure S7) rather than seasonality; while we suspect that microbial metabolisms may be driving rapid changes in carbonate chemistry, and thus carbonate precipitation, the rate of carbonate production is likely not high enough to drive resolvable differences in carbonate isotopic compositions between sampling seasons in this study. However, multiple lines of evidence suggest that both facies found at AI-3 are sensitive to both climate and biology.

Microbial carbon cycling by anaerobic respiration and primary production can influence  $\delta^{13}\text{C}$  of bulk sedimentary organic carbon (Burkhardt, Riebesell, & Zondervan, 1999; Fry & Sherr, 1989; Havig et al., 2018). Previous studies have reported the  $\delta^{13}\text{C}$  values of some of the major organic carbon inputs in GSL: C3/C4 plants (~-26‰ and -13‰ VPDB, respectively; Leng & Marshall, 2004), lacustrine algae which is typically in equilibrium with atmospheric  $\text{CO}_2$  (-7‰ to -8‰ vs. VPDB; Meyers, 1994), and *Artemia* (brine shrimp; -15.1‰ vs. VPDB; Spero, Andreasen, & Sorgeloos, 1993). Additional organic carbon contributors that, to the best of our knowledge, have not been isotopically characterized are bird feces and primary productivity by cyanobacteria in the water column and shallow sediments. Sedimentary organic matter components (e.g., carbohydrates, lipids, amino acids) have different reactivities, and therefore, the source character of total organic carbon may be selectively modified by preferential degradation or respiration of certain molecules (Kawamura & Kaplan, 1987; Meyers, Leenheer, Eaoie, & Maule, 1984). At AI-3, there is a core-specific correlation between  $\delta^{13}\text{C}_{\text{carb}}$  and  $\delta^{13}\text{C}_{\text{org}}$  (Figure S3a). The correlation between  $\delta^{13}\text{C}_{\text{carb}}$  and  $\delta^{13}\text{C}_{\text{org}}$  in the proto-wackestones and quartz proto-sandstones at AI-3 suggests that the isotopic composition of the organic carbon pool in this microenvironment, and in turn, facies is intimately related to authigenic carbonate production. On the contrary, there is no evidence for correlation between  $\delta^{13}\text{C}_{\text{carb}}$  and  $\delta^{13}\text{C}_{\text{org}}$  in the proto-boundstones or grainstones, which we interpret as further evidence that most of the carbonate within these facies is much older than the organic matter preserved in the sediments today and any modern cycling between the organic carbon and carbonate pools is outweighed by the mass of older carbonate. DIC composition is partially derived from the composition of the organic carbon components oxidized by microbial metabolism within sedimentary pore spaces. Both  $\delta^{13}\text{C}_{\text{org}}$  and  $\delta^{13}\text{C}_{\text{DIC}}$  are slightly more variable in AI-3 both by depth (Figure 5) and between the three cores (Figure S3) than at other sites, although there is no clear correlation between  $\delta^{13}\text{C}_{\text{org}}$  and  $\delta^{13}\text{C}_{\text{DIC}}$ . The correlation between organic and carbonate carbon, but not DIC, could indicate that DIC created from microbial organic matter degradation is quantitatively consumed in the precipitation of authigenic carbonate in subsurface porespaces.

We used light and electron microscopy to identify microfabrics indicative of syngenetic or early diagenetic subsurface microbial processes which may alter the primary environmental signal (e.g.,

microbially mediated carbonate precipitation) recorded by carbonate. Previous studies have reported that a close association of amorphous calcium carbonate (ACC) with EPS excreted by cyanobacteria may be indicative of microbially mediated carbonate precipitation (Obst et al., 2009; Shiraishi et al., 2017). Others have suggested that the degradation of EPS and other microbial organic matter by sulfate-reducing bacteria (SRB) might drive carbonate precipitation by locally increasing alkalinity, in which case the loci of carbonate precipitation occur in anoxic zones inhabited by microbes, that is, beneath the surface of a microbial mat or other stratified microbial community (Dupraz et al., 2004; López-García et al., 2005; Pace et al., 2016). Recent observations by Pace et al. (2016) suggest that the latter mechanism may be at play in GSL microbialites.

Our microscopy data revealed evidence for potential microbial-associated carbonate precipitation on quartz grains at AI-3 (Figure 2d). At a depth of 4 cm, we observed putative coccoid cyanobacteria encased in authigenic carbonate on the surface of quartz grains in thin section even though this depth is characterized by  $\Omega_{\text{arag}} < 1$ . Interestingly, carbonate precipitation on bacteria surfaces is energetically beneficial because the forward reaction generates a proton on the outside of cell membranes, thereby creating a proton motive force across the membrane and providing energy for cell activities (Nicholls & Ferguson, 2002):  $\text{Ca}^{2+} + \text{HCO}_3^- \leftrightarrow \text{CaCO}_3 + \text{H}^+$ . In addition, electron microscopy revealed that some quartz grains from the same depth in AI-3 are nearly entirely covered by aragonite crystals (Figure S1c,d) that precipitated in situ after anthropogenic deposition of the quartz sand adjacent to the Antelope Island causeway. The ordered structure of the aragonite blades cannot be categorized as ACC associated with EPS mineralization. We suggest that the aragonite grain coatings, best described as proto-oids (Figure 2h), formed at the sediment surface in contact with lake water ( $\Omega_{\text{arag}} > 1$ ), analogous to ooid formation.

Alternatively, transient increases in alkalinity and  $\Omega_{\text{arag}}$  at depth could be driven by local metabolisms, with  $\Omega_{\text{arag}}$  drawn back down to equilibrium via carbonate precipitation. For example, as discussed in the previous section, MSR and MSO mediate  $\Omega_{\text{arag}}$  by consuming and producing alkalinity, respectively. Both the putrid aroma at the site and abundance of  $\text{Ag}_2\text{S}$  precipitation on the silver strips below 8 cm depth (Figure S4) provide clear evidence of sulfur cycling activity at AI-3. Coincident with this, we see reduced concentrations of sulfate at depth at AI-3 (Figure S2). Furthermore, we find abundant *Desulfo* spp. (SRB) in our 16S rRNA amplicon sequencing analyses (Figure 8). Salinity is overall lower at AI-3 than the other sites due to the freshwater input, which provides a more favorable environment for SRB (e.g., Boyd et al., 2017). In addition, summertime freshwater output from Farmington Bay fuels the production of thick, stringy algal blooms (Figure S8), providing an abundance of organic carbon to be used as electron donors in sulfate reduction and a more reducing environment.

Although the microbial composition of AI-3, SP, and LFP is similar at the sediment–water interface despite very different sedimentary facies at the three sites, the community at 6 cm depth at AI-3 contained abundant Halanaerobaeota, distinct from all other samples.

Halanaerobia are fermentative, anaerobic, halophilic chemoorganotrophs with a wide growth temperature and salinity range. *Halanaerobium praevalens* from GSL are capable of reducing thiosulfate and producing methyl mercaptan as a product of methionine degradation (Zeikus, 1983), properties which may give the AI-3 sediments their distinctive putrid aroma and contribute to carbon isotope compositions. Although the AI-3 and LFP sites are located close together, the AI-3 site sits near the freshwater outlet of Farmington Bay, with its associated high organic load. It is plausible that the distinct community, sediment character, and geochemistry of the two sites are the result of the high TOC in AI-3 sediments (Table S4).

The proximity of site AI-3 to Farmington Bay also plays a role in the oxygen isotope compositions of carbonates at this site. We calculated the equilibrium oxygen isotopic composition of the water from which carbonate samples precipitated using the temperature-dependent fractionation between carbonate and water with measurements of  $\delta^{18}\text{O}_{\text{carb}}$  and  $T(\Delta_{47})$  (Figure 7).  $\delta^{18}\text{O}_{\text{water}}$  of the springs and rivers ( $\sim -15\text{‰ VSMOW}$ ; Newell et al., 2017) that feed GSL are significantly lower than the lakewater ( $\sim -4\text{‰}$  to  $-1\text{‰ VSMOW}$ ; Newell et al., 2017). The calculated  $\delta^{18}\text{O}_{\text{water}}$  values of AI-3 carbonate are more similar to external inputs than lakewater composition demonstrating that authigenic micrite and microbialite intraclasts at AI-3 derive a significant contribution of carbonate oxygen from  $^{18}\text{O}$ -depleted freshwater from the Jordan River and Farmington Bay. Geochronology of shoreline deposits has constrained GSL water elevations as stable at near modern levels ( $\sim 1,277$  m.a.s.l., historic low in 2016) since the Gilbert episode of the Younger Dryas ( $\sim 1,295$  m.a.s.l. at  $\sim 11.5\text{ ka}$ ; Murchison, 1989). Therefore, we would not expect significant differences in carbonate isotope values based on paleo-aridity alone over the duration in which any of the carbonate materials sampled in this study precipitated. If the micritic grain coatings from AI-3 precipitated in equilibrium with the mean composition of lakewater, we would expect  $\delta^{18}\text{O}_{\text{carb}}$  and  $\delta^{13}\text{C}_{\text{carb}}$  values to be comparable to the time-averaged compositions of the ooid samples. Therefore, both the microbialite intraclasts and carbonate mud of the proto-wackestone and carbonate grain coatings of the proto-sandstone are sensitive to local hydrological inputs.

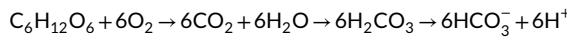
In addition to the relatively low  $\delta^{18}\text{O}_{\text{water}}$  values calculated from AI-3 carbonate samples, clumped isotope temperatures significantly lower than the other sites corroborates that AI-3 micrite formed in equilibrium with cold freshwater derived from the Jordan River rather than mean lakewater. Simultaneously, higher altitude (lower  $\delta^{18}\text{O}$ ) meteoric water from within the drainage basin is introduced to the lacustrine carbonate record.

Most  $\Delta_{47}$  values from AI-3 yield reasonable temperatures for carbonate forming in equilibrium with a mixture of lakewater and colder river water ( $\sim 2$  to  $10^\circ\text{C}$ ; Table 2; Figure 7); however, micrite from 1 cm below the sediment–water interface in Fall 2018 yields a  $T(\Delta_{47})$  of  $-11 \pm 4^\circ\text{C}$ , which is unreasonable even for high altitude river water and saline lake water. Sediment from 6 cm depth yields a  $T(\Delta_{47})$  of  $2.6^{+4.8}_{-4.6} \text{ }^\circ\text{C}$ , which is the next lowest temperature (highest  $\Delta_{47}$ ) of the entire dataset. We suggest that metabolisms associated with the microbial community at AI-3 cause rapid changes in

alkalinity, and thus  $\Omega_{\text{arag}}$ , invoking a kinetic isotope effect yielding higher  $\Delta_{47}$  values than carbonates forming in equilibrium with respect to  $\Delta_{47}$ .

Most previous work has sought to explain negative  $\Delta_{47}$  anomalies away from Earth surface precipitation conditions, such as high temperature burial diagenesis (e.g., Stolper & Eiler, 2015) and the effects of anaerobic oxidation of methane on the DIC system (Loyd et al., 2016). However, recent work has demonstrated that perhaps  $\Delta_{47}$  alteration and disequilibrium is not, in fact, unidirectional and  $\Delta_{47}$  can be pulled to anomalously high values during fast mineral growth (Daeron et al., 2019) or the slow interconversion of  $\text{CO}_2$  and  $\text{HCO}_3^-$  in the  $\text{DIC-H}_2\text{O-CO}_2$  system (Guo, 2020; see Appendix S1). These enrichments and depletions are enhanced when mixing two DIC pools with similar  $\Delta_{47}$  composition but distinct bulk carbon and oxygen compositions (Guo, 2020), as we might expect when mixing Farmington Bay freshwater with GSL water. However, the temperature calculated from the  $\Delta_{47}$  value is physically implausible even considering meltwater mixing (Figure 7), and the amount of  $\Delta_{47}$  enrichment is not beyond the realm of disequilibria (see discussion in the Appendix S1 for details). Thus, if a  $\Delta_{47}$  value falls outside of the statistical distribution of all other measurements at a site and yields an unreasonably cold  $T(\Delta_{47})$ , it is perhaps likely that carbonate precipitated out of  $\Delta_{47}$  thermodynamic equilibrium with the mean aqueous environment mediated by rapid microbial mediation of carbonate chemistry.

Notably,  $\Omega_{\text{arag}}$  is also highest at 1 cm depth where there is potential authigenic  $\Delta_{47}$  disequilibrium. The  $\Omega_{\text{arag}}$  of  $\sim 4$ , which is elevated over lakewater  $\Omega_{\text{arag}}$ , supports the interpretation based on the  $\Delta_{47}$  value that the carbonate chemistry at this depth is out of equilibrium and high  $\Omega_{\text{arag}}$  is perhaps a transient condition due to rapid metabolic activity. For example, pH, carbonate speciation, and  $\Omega$  are controlled by the balance of [DIC] and alkalinity at each depth, which are in turn controlled by perturbations in community composition and principal metabolic pathways. Overall, [DIC] increases with depth at Al-3 while pH decreases, except for at 1 cm depth, where [DIC] is higher than above and below (Figure 8b). The increase in [DIC] and  $\Omega_{\text{arag}}$  at 1 cm requires a net reaction that increases alkalinity more than [DIC], while the increase in [DIC] and decrease in  $\Omega_{\text{arag}}$  at 6 cm require a net reaction that increases [DIC] but does not substantially change alkalinity. For example, during aerobic respiration, [DIC] increases while alkalinity is unchanged, thereby decreasing  $\Omega_{\text{arag}}$  (Figure 4a):



However, at both 1 and 6 cm, obligate and facultative anaerobes dominate the 16S operational taxonomic units, suggesting that aerobic respiration is unlikely to be responsible for the increase in [DIC]. During anaerobic respiration, organic matter (e.g., glucose, above), nitrate, or sulfate are used as terminal electron acceptors rather than oxygen; these reactions increase [DIC] without changing alkalinity. As described in the previous section, subsequent sulfur oxidation is required to increase alkalinity and

$\Omega_{\text{arag}}$  after MSR. A higher frequency of the anoxygenic phototrophic sulfur oxidizer *Chloroflexi* (Kubo, Knittel, Amann, Fukui, & Matsuura, 2011) occurs in the sample from Al-3 1 cm (Figure 8). On the contrary, the SRB *Halanaerobium* (Booker et al., 2017; Ravot et al., 1997) is by far the most abundant genus found in the 6 cm sample. Thus, we suggest that sulfur oxidation locally, and potentially rapidly, increases alkalinity sufficiently to increase  $\Omega_{\text{arag}}$  above that of ambient lake water in the near subsurface, while MSR and other anaerobic respiration pathways decrease  $\Omega_{\text{arag}}$  at depth. At these lower depths,  $\Omega_{\text{arag}} \lesssim 1$ , inhibiting precipitation of authigenic carbonate.

In summary, authigenic micrite records localized physicochemical conditions and biological activity in porespace microenvironments. Based on the positive, yet shifting, carbonate  $\delta^{13}\text{C}-\delta^{18}\text{O}$  correlation, we find that thin grain coatings and other authigenic carbonates record local hydrological inputs and have the potential to record discrete climate events. Further, the implausibly low clumped isotope temperatures and potential disequilibrium  $\Delta_{47}$  values demonstrate that thin micrite grain coatings and other authigenic carbonates are prone to kinetic isotope fractionations from local biological processes. Additional process-based experimental work must be done before a specific microbially mediated reaction can definitively be assigned as the driver of  $\Delta_{47}$  disequilibrium behavior at GSL. However, taking disequilibrium  $\Delta_{47}$  values at face value in the modern or, more important, in the rock record would result in incorrect interpretations of  $\Delta_{47}$  values as true carbonate formation temperature estimates.

#### 4.1.3 | Microbialite and intraclasts at Ladyfinger Point

Microbial mediation of carbonate chemistry and its impact on the isotopic record is most evident at LFP, both at the sediment–water interface and at depth, despite the observation that LFP porewater is strongly undersaturated with respect to aragonite (Figure 4b). First, LFP hosts dozens of thrombolitic mounds (Figure 1d,h,i) with active photosynthetic microbial communities living on the exterior and non-photosynthetic communities living within the microbialite interior (Figure 8). Shoreline thrombolites experience intermittent subaerial exposure during seasonal lake level fluctuations (Figure 1i). We sampled both carbonate and DNA from subaerial and subaqueous mounds in Fall 2018 to characterize changes in the community structure during these seasonal shifts in environmental conditions and to observe whether community change could be responsible for variability in carbonate material preserved in the rock record.

Although differences were observed based on date, site, and depth, weighted UniFrac and Bray–Curtis dissimilarity scores generally grouped microbialite samples together (Figure 9, Figure S7), and indicated that microbialite communities are distinct from sediment samples from LFP and elsewhere (Figure 9). LFP microbialite interior samples from both October 2017 and October 2018 formed

a distinct group, indicating a stable community. The abundance of Anaerolineaceae sequences in the microbialite interior is suggestive of the potential for methanogenesis within the microbialites (Liang et al., 2015).

Ladyfinger Point microbialite exterior samples showed greater spatial, and potentially temporal, variability than interior samples (Figure 8). Microbialite exterior samples collected in 2011 and analyzed by Lindsay et al. (2017) had a substantially different microbial community relative to our exterior microbialite sample. Lindsay et al. (2017) found abundant Alteromonadales and Oceanospirales, which were only a very small portion of the microbialite surface communities in our study. However, the cyanobacterium identified in the Lindsay study was classified as having 100% sequence identity (using a different primer set) to *Euhalotheca* sp. MPI 96N304, which is a member of the same *Dactylococcopsis* PCC8305 group that the abundant cyanobacterial ASVs of our study belonged to. The most similar sequence in the NCBI BLAST® database (<https://blast.ncbi.nlm.nih.gov/Blast.cgi>, accessed October 2019) to the most abundant cyanobacterial ASV was an uncultured cyanobacterium from a hypersaline mat from Guerrero Negro (GenBank JN513594.1; 99.3% sequence similarity). Members of this group are found in shallow saline environments worldwide and are notable for their tolerance of high light intensities (Walsby, Van, & Cohen, 1983). Among other abundant sequences in our samples were those identified as diverse Saprospiraceae (members of which break down complex organic molecules; McIlroy & Nielsen, 2014), Psychoflexus (many members of which are halophilic heterotrophs; e.g., (Dorador et al., 2009; Zhong et al., 2016), and Rhodobacteraceae (photo- and chemoheterotrophs; Pujalte, Lucena, Ruvira, Arahal, & Macián, 2014). The near absence of sequences classified as  $\delta$ -Proteobacteria (including *Desulfo*- spp.) in microbialite exterior samples and their abundance in interior samples is consistent with anaerobic conditions and sulfur cycling—particularly sulfate reduction—in the interior of microbialites, as demonstrated by Pace et al. (2016). The observed  $\text{Ag}_2\text{S}$  precipitation on the silver strips placed at LFP provide further evidence of abundant sulfate reduction occurring below the sediment–water interface within sediment pore spaces.

Sulfate reducing bacteria-associated organomineralization has been implicated in the formation of chemically complex aragonite-dolomite-silicate authigenic mineral assemblages at GSL (Pace et al., 2016) that are not primary lake deposits that could have precipitated from the lake water chemistry alone. We identified hemispherical voids permineralized with magnesium-silicate spherules within microbialite intraclasts collected at 4 cm depth in Fall 2017 (Figure S1). These clusters of aragonite-coated Mg-Si spherical aggregates are similar in shape and size to coccoid cyanobacteria (5–10  $\mu\text{m}$  diameter) and thus are assumed to be casts of degraded coccoidal cells. Pace et al. (2016) proposed a model in line with our findings for LFP 4 cm samples, where a secondary magnesian clay, stevensite, which is favored under high salinity conditions (Pozo & Calvo, 2018), is found in association with aragonite-coated coccoid voids and “hot spots” of sulfate reduction activity. The coccoid voids in the LFP microbialite intraclasts are found at the same depth as the

greatest amount of  $\text{Ag}_2\text{S}$  precipitation in our sulfate reduction field incubations (4 cm). The independent evidence for sulfate reduction at the same depth and location as the highest  $\delta^{13}\text{C}_{\text{carb}}$  value in the entire dataset (Figure 5) could implicate sulfur cyclers as players in the mediation of carbonate chemistry and the carbon isotope system within this microenvironment. Any amount of authigenic carbonate formation at depth at LFP requires  $\Omega_{\text{arag}} > 1$ , but  $\Omega_{\text{arag}}$  was less than 1 in the Spring 2018 porewaters. Our microscopy data therefore suggest that  $\Omega_{\text{arag}}$  was greater than 1 at other times, perhaps due to seasonal changes in community composition, local metabolism, and environmental conditions (e.g., temperature or freshwater input).

Production of  $\text{CO}_2$  resulting from microbial respiration contributes carbon to the lacustrine DIC system. Biological fractionation during microbial carbon cycling can influence the atmospheric  $\text{CO}_2$ -buffered DIC system (Guy, Fogel, & Berry, 1993; Robinson et al., 2003; Roeske & O’Leary, 1985) and, in turn,  $\delta^{13}\text{C}_{\text{carb}}$ . As such, carbonates precipitating from a microbially influenced DIC pool will not necessarily follow the positive correlation between carbonate  $\delta^{18}\text{O}_{\text{carb}}$  and  $\delta^{13}\text{C}$  expected in closed basin lakes. At LFP, we find no statistically significant correlation between  $\delta^{18}\text{O}_{\text{carb}}$  and  $\delta^{13}\text{C}_{\text{carb}}$  (Figure 6c), but instead find a large range of  $\delta^{13}\text{C}_{\text{carb}}$ . We hypothesize that the wide range of  $\delta^{13}\text{C}_{\text{carb}}$  in GSL microbialites without an associated change in  $\delta^{18}\text{O}_{\text{carb}}$  indicates that  $\delta^{13}\text{C}_{\text{carb}}$  is controlled more by microbial carbon cycling than typical controls, that is, hydroclimate, local hydrology, and atmospheric  $\text{CO}_2$ .

In the proto-boundstone and packstone facies,  $\delta^{13}\text{C}_{\text{carb}}$  ranges overall from 1.3‰ to 10.1‰, with each of the three cores comprising discrete populations. The relatively large isotopic shifts at LFP could be driven by local microbial metabolism within subsurface microenvironments and potentially community succession due to seasonal changes in water depth and temperature. Interestingly, the changes in  $\delta^{13}\text{C}_{\text{carb}}$  hypothesized to be driven by changes in microbial activity between seasons and/or sampling sites does not seem to be recorded in the  $\delta^{13}\text{C}$  of bulk organic matter, as there is no significant correlation between  $\delta^{13}\text{C}$  of organic matter and carbonate between seasons (Figure S3). As such, we believe much of the spread  $\delta^{13}\text{C}_{\text{carb}}$  in the boundstone and packstone facies could be explained by spatial heterogeneity in the community and sedimentary composition of the upper 12 cm below the sediment–water interface between coring sites at LFP and that the bulk of the microbialite and microbialite intraclast material is older than the modern microbes colonizing microbialite surfaces and sedimentary porespaces.

In contrast to carbon isotopes,  $\delta^{18}\text{O}_{\text{carb}}$  values of LFP microbialite and microbialite intraclasts are statistically indistinguishable between the 2017–2018 coring sites, and fall within the restricted range of the ooid sites (−5.2‰ to −3.8‰ VPDB; Figures 5 and 6). The Spring 2018 LFP core yields slightly higher  $\delta^{18}\text{O}_{\text{carb}}$  values than samples collected in the two Fall LFP cores, which could reflect the impact of seasonal lake level fluctuations on oxygen isotope values of the minimal amount of authigenic carbonate—that is, carbonates precipitating from evaporatively  $^{18}\text{O}$ -enriched lakewater during seasonal lowstands will record higher  $\delta^{18}\text{O}_{\text{carb}}$  values. This is also the seasonal  $\delta^{18}\text{O}_{\text{carb}}$  trend observed between AI-3 cores. However, this

would require higher rates of authigenic carbonate production in the relatively short interim between coring seasons, for which we do not find petrographic evidence. As such, the relatively small variation in  $\delta^{18}\text{O}_{\text{carb}}$  between LFP core sites likely reflects the previously described spatial heterogeneity at LFP, and a higher concentration of microbialite intraclasts that originally formed during a lowstand period. Regardless of precipitation timing, unlike the proto-oid grain coatings, GSL microbialites precipitate in equilibrium with the lakewater  $\delta^{18}\text{O}_{\text{water}}$  based on calculations from  $\delta^{18}\text{O}_{\text{carb}}$  and  $T(\Delta_{47})$  and lakewater measurements from Newell et al. (2017). Calculated clumped isotope temperatures of the proto-packstone and microbialite boundstone facies are indistinguishable from the proto-grainstone facies and slightly lower than field water temperature measurements from the sampling seasons (Figure 7).

In summary, proto-packstone and microbialite boundstone facies at LFP record  $\delta^{18}\text{O}_{\text{carb}}$  and  $\Delta_{47}$  values in equilibrium with lake water, but are seemingly heterogeneous in terms of  $\delta^{13}\text{C}_{\text{carb}}$  values. This heterogeneity is likely due to a combination of spatial heterogeneity in microbial communities between microenvironments at LFP, and potentially seasonal changes in the influence of microbial processes acting on the DIC system; these seasonal shifts are likely due to shifts in community composition on microbialite surfaces during periods of subaqueous versus subaerial exposure, but are suspected to contribute a minimal mass fraction to the total carbonate in the system.

## 4.2 | Leveraging multiple carbonate components within a lacustrine basin to reconstruct a broader regional climatic, hydrological, and biological history

At GSL, the isotopic values recorded by different lacustrine carbonate components (e.g., ooids, microbialites, intraclast and authigenic grain coatings, and mud) record different characteristics of the greater lake system: snapshots of lakewater chemistry, local hydrological inputs from the greater drainage basin and regional hydroclimate, and local biological processes. With a better understanding of how each facies records environmental and microbial processes, facies-specific isotopic measurements of lacustrine stratigraphy can be leveraged to reconstruct both local lacustrine hydrology (e.g., evaporation–precipitation balance) as well as regional climate and hydrology across the greater drainage basin, and infer candidate microbial processes that may have played a role in carbonate formation and alteration in an ancient lake system.

### 4.2.1 | Hydrology and climate

We conclude that oolitic grainstone (BB, SJ, SP), packstone (LFP), and microbialite boundstone (LFP) facies record the equilibrium oxygen isotope composition of lake water through time. The carbonate oxygen isotope values of materials from SP, SJ, BB, and LFP are comparable between seasons, and calculations of  $\delta^{18}\text{O}_{\text{water}}$  from  $\delta^{18}\text{O}_{\text{carb}}$  are

similar to lakewater. These calculated  $\delta^{18}\text{O}_{\text{water}}$  values are systematically lower than lake water measured by Newell et al. (2017), which could be due to particularly evaporatively enriched water sample collected in Spring 2015 by Newell and colleagues, or be an artifact of the time averaging nature of ooid laminae that accumulated over a few thousand years (Paradis et al., 2017) and microbialite intraclasts that formed sometime during those few thousand years or earlier (Newell et al., 2017). Mean lake level has not changed significantly since the Gilbert episode of the Younger Dryas (~11.5 ka; Oviatt, 2015), and thus, we would not expect mean  $\delta^{18}\text{O}_{\text{water}}$  to have significant interannual variation. However, shallow, closed-basin lakes can have significant seasonal fluctuations in  $\delta^{18}\text{O}_{\text{water}}$  (e.g., Dincer, 1968; Henderson & Shuman, 2009; Steinman et al., 2013). As such, even though the 2015 lakewater measurements are a few permill more  $^{18}\text{O}$ -enriched than the calculated values from paired  $\delta^{18}\text{O}_{\text{carb}}$  and  $T(\Delta_{47})$  of ooids and microbialite, these substrates provide robust records of mean basin hydrology at the time of carbonate precipitation and over geologically meaningful intervals. Thus, oolitic proto-grainstone, proto-packstone, and microbialite proto-boundstone facies can be used for calculations of evaporation–precipitation balance and to inform ancient climate models when the facies-specific isotopic data are interpreted within the framework of time integrated carbonate formation.

The authigenic aragonite coatings on detrital quartz at Al-3 can be viewed as proto-oids. As such, each lamination records the water oxygen and DIC compositions at the time of carbonate precipitation. At Al-3, the recent individual grain coatings seem to record the water isotopic composition of external water sources within the drainage basin. Thus, thin, micritic grain coatings in sandstone facies can be leveraged to glean information about the regional hydroclimate, and potentially basin hypsometry if the low  $\delta^{18}\text{O}_{\text{water}}$  values are significantly light enough to indicate higher altitudes within the basin, as in the case of the rivers feeding GSL. Further, micritic grain coatings, carbonate mud, and microbialite intraclasts from Al-3 yields the strongest correlation between  $\delta^{18}\text{O}_{\text{carb}}$  and  $\delta^{13}\text{C}$  of all the carbonate types, as expected in closed basin lakes. Although external fresh water sources contribute to the  $\delta^{18}\text{O}_{\text{water}}$  at Al-3, the authigenic grain coatings remain sensitive to lake level changes that drive evaporative enrichment and positive  $\delta^{18}\text{O}_{\text{carb}}-\delta^{13}\text{C}_{\text{carb}}$  correlation. In summary, thin carbonate grain coatings and micritic intraclasts are likely the best recorders of closed basin hydrological conditions because smaller carbonate grain sizes can rapidly precipitate out of solution, and thus, do not have the time averaging effect of larger ooid grains and whole microbialite mounds. Instead, the proto-wackestone and proto-sandstone facies record a brief window into lake water chemistry and evaporation–precipitation balance.

### 4.2.2 | Sedimentary record of lacustrine communities

When cells or their imprints are preserved in the rock record, we can make inferences about the microbial community present in an

ancient system based on cellular morphology (e.g., Mata et al., 2012 and references therein). For instance, at 4 cm depth at LFP, we find putative casts of degraded coccoid cyanobacteria which could potentially be preserved after lithification. In the absence of preserved cellular material or casts, there is no direct optical method for identifying who lived in a past depositional environment. However, microbial biomass, which makes up a significant fraction of particulate organic carbon (POC), can be preserved in the sedimentary record in areas of high POC sedimentation and burial. The carbon isotopic composition of microbial biomass is set by the composition of the inorganic carbon used by cells during carbon fixation and the fractionations associated with specific carbon fixation pathways. Thus, sedimentary environments with high microbial diversity could record a larger range of  $\delta^{13}\text{C}_{\text{org}}$  than environments with stable microbial communities.

Samples from the ooid-dominated facies have homogenous communities within a given site as evidenced by small calculated sample community distances within single sites. AI-3 and LFP, conversely, had distinct communities at different sampling depths and for different sample types (Figure 9, Figure S7). AI-3 experiences substantial environmental perturbations between seasons due to seasonal influx of freshwater from the Jordan River and Farmington Bay. In the spring melt season, salinity and water temperature at AI-3 are relatively low as cold freshwater is introduced across the causeway. By the fall, the influx of meltwater is significantly lower, and salinity is higher. Changes in salinity are evidenced by seasonal concentrations of dissolved sodium and chloride concentrations (Figure S2). A sample from 6 cm depth at AI-3 was dominated by *Halanaerobium*, an obligate anaerobe and known sulfur cycler that can tolerate high salinity–high pH environments (Booker et al., 2017). Some strains of *Halanaerobium* are known to generate  $\text{H}_2\text{S}$  in the presence of thiosulfate, which was qualitatively observed in AI-3 samples via ion chromatography. During Fall 2018, when sediments were collected for 16S analyses, the same 6 cm sample with abundant *Halanaerobium* ASVs also produced  $\delta^{13}\text{C}_{\text{org}}$  values ~1.5‰ lower than  $\delta^{13}\text{C}_{\text{org}}$  of the upper sample. This significant difference in organic  $\delta^{13}\text{C}_{\text{org}}$  values between proximal sites is likely due to the metabolic pathways undertaken in aerobic (upper) versus anaerobic (lower) environments. In addition to the 1.5‰ range measured in the Fall 2018 samples, there is a total range of ~3.5‰ between all depths and three seasons with the greatest difference being between Fall 2017 and Spring 2018. Again, this seasonal difference can likely be linked to the freshwater pulse from Farmington Bay in the spring that also brings a high organic load, producing an algal bloom and increasing the rate of POC sedimentation.

The variable hydrology at AI-3 facilitates biologically significant variability in dissolved organic carbon (DOC) content, oxygen levels in the water column and in the sediments, and light availability. Diversity seems to be mirrored in the seasonal variability in  $\delta^{13}\text{C}_{\text{org}}$  at AI-3, which should be preserved in the eventual GSL rock record. In the previous section, we discussed how micritic facies preserve seasonal and spatial differences in carbonate chemistry and carbonate

stable isotopes due to climatic and hydrological variability, recording a snapshot of carbonate chemistry and water composition at the time of increased  $\Omega_{\text{arag}}$  and carbonate precipitation. Likewise, variability in organic carbon isotopes partnered with the presence of micrite in the lacustrine sedimentary record could indicate a site with greater microenvironmental variability than other sites within the same basin, and correspondingly greater beta diversity in the microbial community.

Surface and deep samples at LFP, as well as exterior and interior samples of microbialite mounds, also yield diverse community data. The  $\delta^{13}\text{C}_{\text{org}}$  end members of the 2‰ range at LFP are from 4 cm and 8 cm depths of the Fall 2017 core. The Fall 2017 4 cm sample is also where we found evidence of EPS degradation and organomineralization potentially related to sulfate reduction (Figure S1). Although the 16S rRNA data are not from the Fall 2017 core, we expect that similar differences in microbial population between depths would be found in the Fall 2017 core as in Fall 2018. As such, we hypothesize that different carbon fixation pathways undertaken by unique communities within depth-specific microenvironments produce DOC with variable  $\delta^{13}\text{C}_{\text{org}}$  values.

In addition, carbonate samples from LFP are predominantly microbialites and microbialite intraclasts and, thus, can be expected to host different microbial communities and yield a different organic carbon composition than the ooid sites. The clearest example can be seen at GSL State Park where the microbialites collected in Fall 2018 yield  $\delta^{13}\text{C}_{\text{org}}$  values ~2‰–3‰ higher than ooids collected in Spring 2018 (Figure 5). The surface communities at SP and LFP are different but the same *Desulfo*-spp. sequences are found in the interiors of microbialite mounds at both sites. The photosynthetic bacteria that thrive on the surfaces of the mounds found at SP and LFP fix inorganic carbon by different pathways with different fractionations than the communities of anaerobic or non-photosynthetic communities that thrive in the subsurface. As such, comparable magnitude differences in  $\delta^{13}\text{C}_{\text{org}}$  between proximal samples in the rock record, when taken within the context of lithology, could demonstrate that different metabolisms existed within microenvironments of the same facies. As at AI-3, the spread in  $\delta^{13}\text{C}_{\text{org}}$  values at LFP is indicative of spatial and lithology-specific microbial diversity, or possibly seasonal succession.

#### 4.2.3 | An example of interpreting variability across a sedimentary horizon

Thus far, we have discussed how early diagenetic processes or localized differences in surface hydrology may manifest as significant isotopic excursions in the sedimentary record. A single sedimentary stratum should record a snapshot in an environment's depositional history. As such, to characterize change in an isotopic or geochemical system of interest in an ancient lacustrine basin through time, one or two stratigraphic sections are typically measured, described, and sampled. This type of focused sampling works under the assumption that each lacustrine

horizon records the mean lakewater chemistry, hydrology, and biology of the system at the time of sedimentation. However, our test of this assumption has demonstrated that unique carbonate lithologies and sedimentary regimes across a single lake basin are sensitive to different characteristics of the lake system (i.e. biology versus hydrology), and do not all record the mean hydroclimatic or biological state of the lake. The modern GSL sediment-water interface is an example of a single sedimentary horizon of relatively coeval sediments yielding ranges in  $\delta^{18}\text{O}_{\text{carb}}$ ,  $\delta^{13}\text{C}_{\text{carb}}$ ,  $\delta^{13}\text{C}_{\text{org}}$ , and  $\delta^{13}\text{C}_{\text{DIC}}$  of  $5.1\text{\textperthousand}$ ,  $5.9\text{\textperthousand}$ ,  $2.4\text{\textperthousand}$ , and  $8.1\text{\textperthousand}$ , respectively (Figure 10). In the rock record, this variability could be inaccurately interpreted as post-burial, late-stage diagenesis rather than variability in hydrological inputs and biologically mediated eogenesis.

Our study highlights the danger of assigning a single isotopic value to an entire depositional horizon for the purposes of interpreting depositional environments without sampling multiple stratigraphic sections across a laterally extensive basin to assess lateral variability. For example, using the carbonate oxygen isotope thermometer of Kim and O'Neil, (1997):  $1,000 \ln \alpha_{\text{CaCO}_3-\text{H}_2\text{O}} = \frac{18.030}{T} - 32.42$ , where  $\alpha = (1,000 + \delta^{18}\text{O}_{\text{carb}})/(1,000 + \delta^{18}\text{O}_{\text{water}})$ , we can assign a lakewater  $\delta^{18}\text{O}_{\text{water}}$  value

of  $-4\text{\textperthousand}$  vs. VSMOW (Newell et al., 2017) and the end member  $\delta^{18}\text{O}_{\text{carb}}$  values from Bridger Bay and Al-3 ( $-4.1\text{\textperthousand}$  and  $-9.2\text{\textperthousand}$  vs. VPDB) at the sediment-water interface and calculate equilibrium temperatures of  $14.1$  and  $39.7^\circ\text{C}$ , respectively. This magnitude of variance at the sediment-water interface demonstrates that local hydrological effects and microenvironmental processes can cause significant isotopic variability across a single depositional horizon. Exhaustive lateral sampling is likely necessary to characterize this variability and make robust assessments of the environmental conditions during the deposition of any individual stratum.

The actual range of clumped isotope-derived temperatures at the sediment-water interface is  $6^\circ\text{C}$ , but all samples agree within uncertainty.  $T(\Delta_{47})$  from LFP, BB, SJ, and SP agree within uncertainty at all depths. Considering this within the framework that LFP microbialite and mud at the sediment-water interface likely precipitated more recently than the ooids, and the ooids record a time-averaged signal, we can interpret the lack of variability in these  $T(\Delta_{47})$  measurements as evidence for relative stability of the temperature and possibly season of carbonate formation in GSL over the last few thousand years.  $T(\Delta_{47})$  of the Al-3 sediment-water interface sample is  $6.7^{+4.9}_{-4.7}{}^\circ\text{C}$ , which is colder than water temperature measured during any of the sampling seasons,

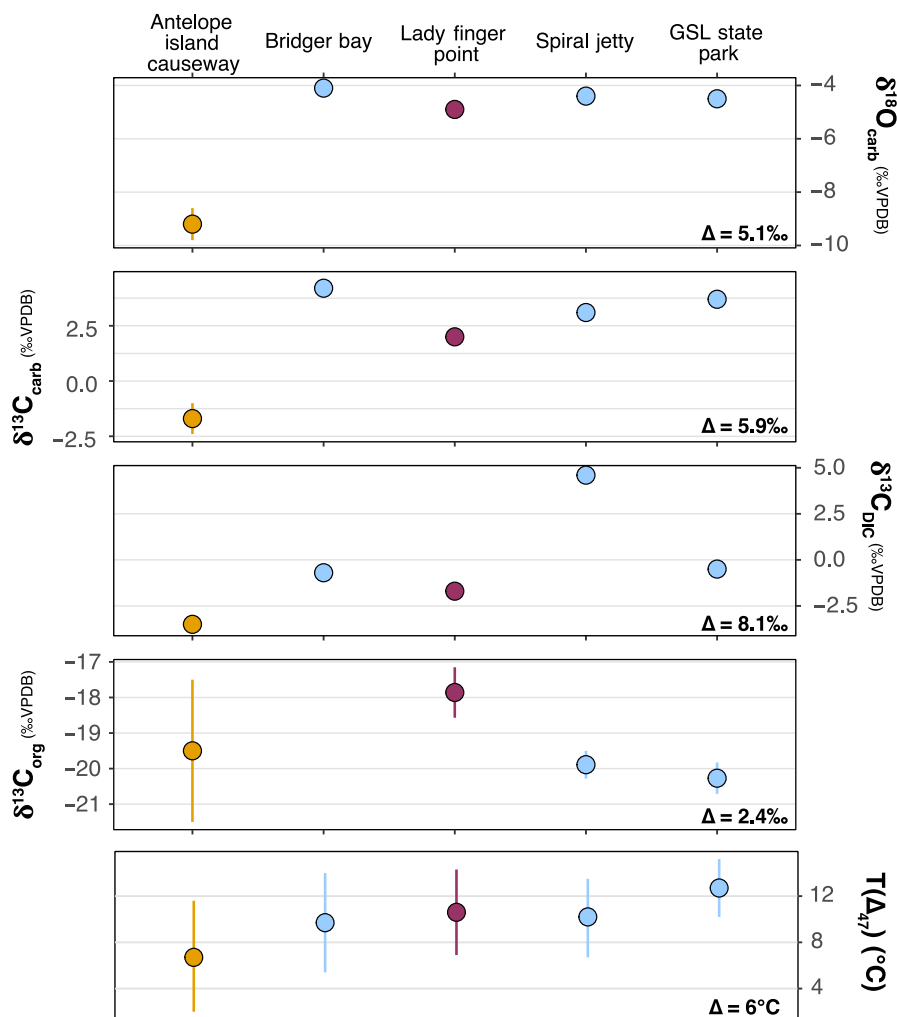


**FIGURE 10** Stable isotopic variability across shoreline coring sites at the sediment-water interface.  $\Delta$  values indicate maximum difference between the five sites for each isotope system. Colors denote facies following previous figures

but not unreasonable for meltwater pulses from Farmington Bay in the winter and early spring. All  $T(\Delta_{47})$  measurements from all sites and depths were at or below the water temperatures measured in Spring 2018 and significantly colder than any Fall 2018 water temperatures. These data provide evidence for either a preference for carbonate formation during the coldest intervals (i.e., seasonal or interannual) in GSL in the modern and recent history, or more likely, subtle microbially driven disequilibria.

## 5 | CONCLUSIONS

In this work, we partnered stable isotope and aqueous geochemistry, microbiology, and carbonate sedimentology to identify syntetic and early diagenetic effects related to microbial processes in modern carbonate lake sediments and ancient sedimentary basins, and to identify biogeochemical cycling between the organic and inorganic reservoirs of carbonate minerals, organic matter, and water. We determined the role of GSL's shoreline microbial communities on local aqueous carbonate chemistry and, in turn, the stable isotopic compositions of recent microbialite, ooids, carbonate mud and authigenic micrite. This work provides a framework for interpreting facies-specific isotopic data from ancient alkaline lakes. Importantly, we found that unique carbonate facies and sedimentary regimes across a single lake basin are sensitive to different characteristics of the lake system (i.e. biology versus hydrology), and do not all record the mean hydroclimatic or biological state of the lake.

Specifically, ooid-dominated facies record a time-averaged isotopic history of GSL water chemistry, and the time-integrated nature of ooid carbonate buffers the bulk isotopic composition from biological processes, but also makes ooids a poor record of century- to millenia-scale intervals of hydrological and climatic change. Microbialite carbonate and intraclasts are robust proxies for  $\delta^{18}\text{O}$  of the lake system, but  $\delta^{13}\text{C}$  values of these components are more sensitive to biological carbon cycling and can yield significant microbial community spatial variability between subsurface microenvironments and between communities growing within and on the surface of microbialite mounds. We concluded that oolitic grainstone (BB, SJ, SP), packstone (LFP), and microbialite boundstone (LFP) facies record the equilibrium oxygen isotope composition of lake water through time. More broadly, carbon and oxygen isotopes of lacustrine carbonates have the power to inform robust paleohydrologic and paleoclimatic reconstructions over geologically meaningful intervals when the facies-specific isotopic data are interpreted within the framework of time-integrated carbonate formation.

Micritic grain coatings, on the other hand, precipitate rapidly and thus their stable isotopic compositions provide snapshots of lake-water chemistry, hydrology, and in some cases, biology. Therefore, micrite sampled stratigraphically should record trends in hydroclimate and basin hydrology, such as changes in evaporation–precipitation balance or changes in freshwater inputs via drainage reconfiguration. However, two micritic grain coatings from Al-3 yielded implausibly

low  $T(\Delta_{47})$  values, with the lowest being  $-11 \pm 4^\circ\text{C}$ ; thus, care should be taken to assess the potential for rapid, biologically mediated carbonate formation that is not in isotopic equilibrium when using this facies.

We suggest that some inflections in the carbon and oxygen isotope record preserved in lacustrine carbonate stratigraphy previously interpreted as regional or global environmental perturbations could be explained by localized, early diagenetic biological processes and authigenic carbonate precipitation. Finally, considering the rock record of ancient lacustrine basins within the context of aforementioned facies-specific isotopic sensitivities, and leveraging multiple facies from contemporaneous stratigraphy, could yield more detailed records of biological activity and succession, and hydrological and climatic change.

## ACKNOWLEDGMENTS

MI would like to thank Usha Lingappa for assistance in performing DNA extraction and amplification, and initial bioinformatics. MI also thanks Chi Ma for assistance with SEM imaging, and Nathan Dalleska for use of the Caltech Environmental Analysis Center, and valuable insight in designing dissolved ion analytical protocols for GSL brines. MI thanks John Eiler for use of clumped isotope facilities at Caltech and discussions of data quality and isotopic disequilibrium. MI and KS thank Brett Davidheiser-Kroll and Andrew Chan for assistance in measurements made in the CUBES-SIL facility and Camsizer analyses. Sampling at Great Salt Lake was carried out under permits to CF from the State of Utah Department of Natural Resources Division of Forestry, Fire and State Lands (No. 42000074) and Antelope Island State Park. Funding for this work was provided by NSF EAR #1826850 to ET and KS and #1826869 to CF. MI acknowledges financial support from the Barr Foundation.

## ORCID

Miquela Ingalls  <https://orcid.org/0000-0002-7451-2944>  
 Carie M. Frantz  <https://orcid.org/0000-0003-2544-9245>  
 Kathryn E. Snell  <https://orcid.org/0000-0001-5373-7143>  
 Elizabeth J. Trower  <https://orcid.org/0000-0001-9898-5589>

## REFERENCES

Baas-Becking, L. G. M. (1934). *Geobiologie*. The Hague, The Netherlands: W.P. Stockum & Zoonp.

Baskin, R. L., & Allen, D. V. (2005). Bathymetric map of the south part of Great Salt Lake, Utah. In *US Geological Survey Scientific Investigations Map, 2894*. <https://doi.org/10.3133/sim2894>. <http://pubs.usgs.gov/sim/2005/2894/>

Baxter, B. K. (2018). Great Salt Lake microbiology: A historical perspective. *International Microbiology*, 21, 79–95.

Benson, L., Currey, D., Lao, Y., & Hostetler, S. (1992). Lake-size variations in the Lahontan and Bonneville basins between 13,000 and 9000 14C yr B.P. *Palaeogeography, Palaeoclimatology, Palaeoecology*, 95, 19–32.

Bolyen, E., Dillon, M., Bokulich, N., Abnet, C., Al-Ghalith, G., Alexander, H., ... Caporaso, G. (2018). Reproducible, interactive, scalable and extensible microbiome data science using QIIME 2. *Nat Biotechnol*, 37, 852–857. <https://doi.org/10.1038/s41587-019-0209-9>

Booker, A. E., Borton, M. A., Daly, R. A., Welch, S. A., Nicora, C. D., Hoyt, D. W., ... Wilkins M. J. (2017). Sulfide generation by dominant halanaerobium microorganisms in hydraulically fractured shales. *mSphere*, 2, 00257-17. <https://doi.org/10.1128/mSphereDirect.00257-17>

Bouton, A., Vennin, E., Amiotte-Suchet, P., Thomazo, C., Sizun, J., Virgone, A., ... Visscher, P. T. (2019). Prediction of the calcium carbonate budget in a sedimentary basin: A "source-to-sink" approach applied to Great Salt Lake, Utah, USA. *Basin Research*, 1-30. <https://doi.org/10.1111/bre.12412>

Bouton, A., Vennin, E., Mulder, T., Pace, A., Bourillot, R., Thomazo, C., ... Visscher, P. T. (2016). Enhanced development of lacustrine microbialites on gravity flow deposits, Great Salt Lake, Utah, USA. *Sedimentary Geology*, 341, 1-12.

Bowen De León, B., Gerlach, R., Peyton, B. M., & Fields, M. W. (2013). Archaeal and bacterial communities in three alkaline hot springs in heart lake geyser basin, yellowstone national park. *Frontiers in Microbiology*, 4, 330.

Boyd, E. S., Yu, R. Q., Barkay, T., Hamilton, T. L., Baxter, B. K., Naftz, D. L., & Marvin-DiPasquale, M. (2017). Effect of salinity on mercury methylating benthic microbes and their activities in Great Salt Lake, Utah. *Science of the Total Environment*, 581-582, 495-506.

Braissant, O., Decho, A. W., Dupraz, C., Glunk, C., Przekop, K. M., & Visscher, P. T. (2007). Exopolymeric substances of sulfate-reducing bacteria: Interactions with calcium at alkaline pH and implication for formation of carbonate minerals. *Geobiology*, 5, 401-411.

Buczynski, C., & Chafetz, H. S. (1991). Habit of bacterially induced precipitates of calcium carbonate and the influence of medium viscosity on mineralogy. *Journal of Sedimentary Petrology*, 61(2), 226-233.

Burkhardt, S., Riebesell, U., & Zondervan, I. (1999). Stable carbon isotope fractionation by marine phytoplankton in response to daylength, growth rate, and CO<sub>2</sub> availability. *Marine Ecology Progress Series*, 184, 31-41.

Chang, Q., Luan, Y., & Sun, F. (2011). Variance adjusted weighted UniFrac: A powerful beta diversity measure for comparing communities based on phylogeny. *BMC Bioinformatics*, 12(1), 118.

Chidsey, T. C., Vanden Berg, M. D., & Eby, D. E. (2015). Petrography and characterization of microbial carbonates and associated facies from modern Great Salt Lake and Uinta Basin's Eocene Green River Formation in Utah, USA. *Geological Society, London, Special Publications*, 418(1), 261-286.

Coplen, T., Brand, W., Gehre, M., Groning, M., Meijer, H., Toman, B., & Verkouteren, R. (2006). New guidelines for d13C measurements. *Analytical Chemistry*, 78, 2439-2441.

Daeron, M., Drysdale, R. N., Peral, M., Huyghe, D., Blamart, D., Coplen, T. B., ... Zanchetta, G. (2019). Most Earth-surface calcites precipitate out of isotopic equilibrium. *Nature Communications*, 10, 1-7.

Dansgaard, W. (1964). Stable isotopes in precipitation. *Tellus*, 16, 436-468.

Decho, A. W., Visscher, P. T., & Reid, R. P. (2005). Production and cycling of natural microbial exopolymers (EPS) within a marine stromatolite. *Palaeogeography, Palaeoclimatology, Palaeoecology*, 219, 71-86.

Deflise, W. F., Hren, M. T., & Lohmann, K. C. (2015). Compositional and temperature effects of phosphoric acid fractionation on Δ47 analysis and implications for discrepant calibrations. *Chemical Geology*, 396, 51-60.

Dennis, K., Affek, H., Passey, B., Schrag, D., & Eiler, J. (2011). Defining an absolute reference frame for 'clumped' isotope studies of CO<sub>2</sub>. *Geochimica et Cosmochimica Acta*, 75, 7117-7131.

Dincer, T. (1968). The use of oxygen 18 and Deuterium concentrations in the water balance Lakes. *Water Resources Research*, 4, 1289-1306.

Dorador, C., Meneses, D., Urtuvia, V., Demergasso, C., Vila, I., Witzel, K. P., & Imhoff, J. F. (2009). Diversity of bacteroidetes in high-altitude saline evaporitic basins in northern Chile. *Journal of Geophysical Research: Biogeosciences*, 114. <https://doi.org/10.1029/2008JG000837>

Dupraz, C., Fowler, A., Tobias, C., & Visscher, P. T. (2013). Stromatolitic knobs in Storr's Lake (San Salvador, Bahamas): A model system for formation and alteration of laminae. *Geobiology*, 11, 527-548.

Dupraz, C., Reid, R. P., Braissant, O., Decho, A. W., Norman, R. S., & Visscher, P. T. (2009). Processes of carbonate precipitation in modern microbial mats. *Earth-Science Reviews*, 96(3), 141-162.

Dupraz, C., Visscher, P. T., Baumgartner, L. K., & Reid, R. P. (2004). Microbe-mineral interactions: Early carbonate precipitation in a hypersaline lake (Eleuthera Island, Bahamas). *Sedimentology*, 51, 745-765.

Eardley, A. J. (1938). *Sediments of Great Salt Lake*. Salt Lake City, UT: AAPG Bulletin.

Eiler, J. M. (2007). "Clumped-isotope" geochemistry—The study of naturally-occurring, multiply-substituted isotopologues. *Earth and Planetary Science Letters*, 262, 309-327.

Faith, D. P., Minchin, P. R., & Belbin, L. (1987). Compositional dissimilarity as a robust measure of ecological distance. *Vegetatio*, 69, 57-68.

Fry, B., & Sherr, E. B. (1989). δ<sup>13</sup>C measurements as indicators of carbon flow in marine and freshwater ecosystem. In P. W. Rundel, J. R. Ehleringer, & K. A. Nagy (Eds.), *Stable isotopes in ecological research*, Vol. 68 (pp. 196-229). New York, NY: Springer.

Ghosh, P., Adkins, J., Affek, H., Balta, B., Guo, W., Schauble, E. A., ... Eiler, J. M. (2006). 13C-18O bonds in carbonate minerals: A new kind of paleothermometer. *Geochimica et Cosmochimica Acta*, 70, 1439-1456.

Guo, W. (2020). Kinetic Clumped Isotope Fractionation in the DIC-H<sub>2</sub>O-CO<sub>2</sub> System: Patterns, Controls and Implications. *Geochimica et Cosmochimica Acta*, 268, 230-257.

Guy, R. D., Fogel, M. L., & Berry, J. A. (1993). Photosynthetic fractionation of the stable isotopes of oxygen and carbon. *Plant Physiology*, 101, 37-47.

Hammes, F., & Verstraete, W. (2002). Key roles of pH and calcium metabolism in microbial carbonate precipitation. *Reviews in Environmental Science and Biotechnology*, 1(1), 3-7.

Havig, J. R., Hamilton, T. L., McCormick, M., McClure, B., Sowers, T., Wegter, B., & Kump, L. R. (2018). Water column and sediment stable carbon isotope biogeochemistry of permanently redox-stratified Fayetteville Green Lake, New York, U.S.A. *Limnology and Oceanography*, 63, 570-587.

Henderson, A. K., & Shuman, B. N. (2009). Hydrogen and oxygen isotopic compositions of lake water in the western United States. *Bulletin of the Geological Society of America*, 121, 1179-1189.

Huntington, K. W., Eiler, J. M., Affek, H. P., Guo, W., Bonifacie, M., Yeung, L. Y., ... Came, R. (2009). Methods and limitations of "clumped" CO<sub>2</sub> isotope (Delta47) analysis by gas-source isotope ratio mass spectrometry. *Journal of Mass Spectrometry: JMS*, 44, 1318-1329.

Ingalls, M., Frantz, C. M., Snell, K. E., & Trower, E. J. (2020). Great Salt Lake 2020 Geobiology MS raw data. <https://doi.org/10.17605/OSF.IO/NK7PB>

Jorgensen, B. B., & Cohen, Y. (1977). Solar Lake (Sinai). 5. The sulfur cycle of the benthic cyanobacterial mats. *Limnology and Oceanography*, 22, 657-666.

Kawamura, K., & Kaplan, I. R. (1987). Dicarboxylic acids generated by thermal alteration of kerogen and humic acids. *Geochimica et Cosmochimica Acta*, 51(12), 3201-3207.

Kelts, K., & Talbot, M. (1990). Lacustrine carbonates as geochemical archives of environmental change and biotic/abiotic interactions. In M. Tilzer & C. Serruya (Eds.), *Large lakes: Ecological structure and function* (pp. 288-314). Berlin, Germany: Springer.

Kim, S.-T., & O'Neil, J. R. (1997). Equilibrium and nonequilibrium oxygen isotope effects in synthetic carbonates. *Geochimica et Cosmochimica Acta*, 61, 3461-3475.

Kubo, K., Knittel, K., Amann, R., Fukui, M., & Matsuura, K. (2011). Sulfur-metabolizing bacterial populations in microbial mats of the Nakabusa hot spring, Japan. *Systematic and Applied Microbiology*, 34(4), 293–302.

Legendre, P., & Legendre, L. (2012). *Numerical ecology* (3rd ed.). Amsterdam, The Netherlands: Elsevier B.V.

Leng, M. J., & Marshall, J. D. (2004). Palaeoclimate interpretation of stable isotope data from lake sediment archives. *Quaternary Science Reviews*, 23, 811–831.

Lettéron, A., Hamon, Y., Fournier, F., Séranne, M., Pellenard, P., & Joseph, P. (2018). Reconstruction of a saline, lacustrine carbonate system (Priabonian, St-Claptes Basin, SE France): Depositional models, paleogeographic and paleoclimatic implications. *Sedimentary Geology*, 367, 20–47.

Li, H. C., & Ku, T. L. (1997).  $\delta^{13}\text{C}$ - $\delta^{18}\text{O}$  covariance as a paleohydrological indicator for closed-basin lakes. *Palaeoclimatology, Palaeoecology: Palaeogeography*, 133, 69–80.

Liang, B., Wang, L., Mbadinga, S., Liu, J. F., Yang, S. Z., Gu, J. D., & Mu, B. Z. (2015). Anaerolineaceae and Methanosaeta turned to be the dominant microorganisms in alkanes-dependent methanogenic culture after long-term of incubation. *AMB Express*, 5(1), 37. <https://doi.org/10.1186/s13568-015-0117-4>

Lindsay, M. R., Anderson, C., Fox, N., Scofield, G., Allen, J., Anderson, E., ... Boyd, E. S. (2017). Microbialite response to an anthropogenic salinity gradient in Great Salt Lake, Utah. *Geobiology*, 15, 131–145.

Lippmann, F. (1973). *Sedimentary carbonate minerals, rocks, and inorganic materials, monograph series of theoretical and experimental studies* (pp. 228). Berlin, Germany: Springer-Verlag.

López-García, P., Kazmierczak, J., Benzerara, K., Kempe, S., Guyot, F., & Moreira, D. (2005). Bacterial diversity and carbonate precipitation in the giant microbialites from the highly alkaline Lake Van, Turkey. *Extremophiles*, 9, 263–274.

Loyd, S. J., Sample, J., Tripati, R. E., Deflise, W. F., Brooks, K., Hovland, M., ... Tripati, A. E. (2016). Methane seep carbonates yield clumped isotope signatures out of equilibrium with formation temperatures. *Nature Communications*, 7, 12274.

Lozupone, C. A., Hamady, M., Kelley, S. T., & Knight, R. (2007). Quantitative and qualitative  $\beta$  diversity measures lead to different insights into factors that structure microbial communities. *Applied and Environmental Microbiology*, 73(5):1576–1585.

Lozupone, C., & Knight, R. (2005). UniFrac: A new phylogenetic method for comparing microbial communities. *Applied and Environmental Microbiology*, 71(12), 8228–8235.

Lyons, W. B., Long, D. T., Hines, M. E., Gaudette, H. E., & Armstrong, P. B. (1984). Calcification of cyanobacterial mats in Solar Lake, Sinai. *Geology*, 12(10), 623.

Martin-Bello, L., Arenas, C., Andrews, J. E., Alonso-Zarza, A. M., & Marca, A. (2019). Lacustrine stromatolites as multi-scale recorders of climate change: Insights from the Miocene Ebro Basin. *Palaeogeography, Palaeoclimatology, Palaeoecology*, 530, 312–329.

Mata, S. A., Harwood, C. L., Corsetti, F. A., Stork, N. J., Eilers, K., Berelson, W. M., & Spear, J. R. (2012). Influence of gas production and filament orientation on stromatolite microfabric. *Palaeos*, 27(4), 206–219.

McIlroy, S. J., & Nielsen, P. H. (2014). The family saprospiraceae. In E. Rosenberg, E. F. DeLong, S. Lory, E. Stackebrandt, & F. Thompson (Eds.), *The prokaryotes: Other major lineages of bacteria and the Archaea* (4th ed., pp. 323–340). Berlin, Germany: Springer.

Meuser, J. E., Baxter, B. K., Spear, J. R., Peters, J. W., Posewitz, M. C., & Boyd, E. S. (2013). Contrasting patterns of community assembly in the stratified water column of Great Salt Lake, Utah. *Microbial Ecology*, 66, 268–280.

Meyers, P. A. (1994). Preservation of elemental and isotopic source identification of sedimentary organic matter. *Chemical Geology*, 114, 289–302.

Meyers, P. A., Leenheer, M. J., Eaoie, B. J., & Maule, S. J. (1984). Organic geochemistry of suspended and settling particulate matter in Lake Michigan. *Geochimica et Cosmochimica Acta*, 48(3), 443–452.

Mohapatra, G. K., & Johnson, R. A. (1998). Localization of listric faults at thrust fault ramps beneath Great Salt Lake Basin, Utah: Evidence from seismic imaging and finite element modeling. *Journal of Geophysical Research*, 103, 10047–10063.

Murchison, S. B. (1989). Fluctuation History of great Salt Lake, Utah during the last 13,000 years. *Limnoaetecnics laboratory technical report 82-2*. National Aeronautics and Space Administration. [https://digitalcommons.usu.edu/govdocs\\_water/12](https://digitalcommons.usu.edu/govdocs_water/12)

Newell, D. L., Jensen, J. L., Frantz, C. M., & Vanden Berg, M. D. (2017). Great Salt Lake (Utah) microbialite  $\delta^{13}\text{C}$ ,  $\delta^{18}\text{O}$ , and  $\delta^{15}\text{N}$  record fluctuations in Lake biogeochemistry since the late Pleistocene. *Geochemistry, Geophysics, Geosystems*, 18, 3631–3645.

Nicholls, D., & Ferguson, S. (2002). *Bioenergetics* (3rd ed.). Cambridge, MA: Academic Press.

Obst, M., Dynes, J. J., Lawrence, J. R., Swerhone, G. D. W., Benzerara, K., Karunakaran, C., ... Hitchcock, A. P. (2009). Precipitation of amorphous  $\text{CaCO}_3$  (aragonite-like) by cyanobacteria: A STXM study of the influence of EPS on the nucleation process. *Geochimica et Cosmochimica Acta*, 73, 4180–4198.

Oehlert, A. M., Lamb-Wozniak, K. A., Devlin, Q. B., Mackenzie, G. J., Reijmer, J. J. G., & Swart, P. K. (2012). The stable carbon isotopic composition of organic material in platform derived sediments: Implications for reconstructing the global carbon cycle. *Sedimentology*, 59, 319–335.

Oehlert, A. M., & Swart, P. K. (2014). Covariance in the sedimentary record. *Nature Communications*, 5, 1–7.

O'Neil, J. R., Clayton, R. N., & Mayeda, T. K. (1969). Oxygen isotope fractionation in divalent metal carbonates. *The Journal of Chemical Physics*, 51, 5547–5558.

Oviatt, C. G. (1997). Lake Bonneville fluctuations and global climate change. *Geology*, 25, 155–158.

Oviatt, C. G. (2015). Chronology of Lake Bonneville, 30,000 to 10,000 yr B.P. *Quaternary Science Reviews*, 110, 166–171.

Pace, A., Bourillot, R., Bouton, A., Vennin, E., Galaup, S., Bundeleva, I., ... Visscher, P. T. (2016). Microbial and diagenetic steps leading to the mineralisation of Great Salt Lake microbialites. *Scientific Reports*, 6, 31495.

Parada, A. E., Needham, D. M., & Fuhrman, J. A. (2016). Every base matters: Assessing small subunit rRNA primers for marine microbiomes with mock communities, time series and global field samples. *Environmental Microbiology*, 18(5), 1403–1414.

Paradis, O., Corsetti, F. A., Bardsley, A., Hammond, D. E., Xu, X., Stamps, B. W., ... Berelson, W. M. (2017). Radial ooids from Great Salt Lake (Utah) as paleoenvironmental archives: Insights from radio carbon chronology and stable isotopes. In: *American Geophysical Union Fall Meeting Abstracts with Programs*.

Parkhurst, D. L., & Appelo, C. A. J. (2013). PHREEQC (Version 3)-A computer program for speciation, batchreaction, one-dimensional transport, and inverse geochemical calculations. Chapter 43 of Section A: *Groundwater in Book 6 Modeling Techniques*. <https://doi.org/10.3133/tm6A43>

Pedone, V. A., & Folk, R. L. (1996). Formation of aragonite cement by nannobacteria in the Great Salt Lake, Utah. *Geology*, 24, 763–765.

Pozo, M., & Calvo, J. P. (2018). An overview of authigenic magnesian clays. *Minerals*, 8, 520.

Pujalte, M. J., Lucena, T., Ruvira, M. A., Arahal, D. R., & Macián, M. C. (2014). The family Rhodobacteraceae. In E. Rosenberg, E. F. DeLong, E. Stackebrandt, S. Lory, & F. Thompson (Eds.), *The prokaryotes: Alphaproteobacteria and betaproteobacteria* (pp. 439–512). Berlin, Germany: Springer.

Quince, C., Lanzen, A., Davenport, R. J., & Turnbaugh, P. J. (2011). Removing noise from pyrosequenced amplicons. *BMC Bioinformatics*, 12(38). <https://doi.org/10.1186/1471-2105-12-38>

Ravot, G., Magot, M., Ollivier, B., Patel, B. K. C., Ageron, E., Grimont, P. A. D., ... Garcia, J. L. (1997). *Haloanaerobium congoense* sp. nov., an anaerobic, moderately halophilic, thiosulfate- and sulfur-reducing bacterium from an African oil field. *FEMS Microbiology Letters*, 147(1), 81–88.

Robinson, J. J., Scott, K. M., Swanson, S. T., O'Leary, M. H., Horken, K., Tabita, F. R., & Cavanaugh, C. M. (2003). Kinetic isotope effect and characterization of form II RubisCO from the chemoautotrophic endosymbionts of the hydrothermal vent tubeworm *Riftia pachyptila*. *Limnology and Oceanography*, 48, 48–54.

Roduit, N. JMicVision: Image analysis toolbox for measuring and quantifying components of highdefinition images. Version 1.3.2. <https://jmicvision.github.io>

Roeske, C. A., & O'Leary, M. H. (1985). Carbon isotope effect on carboxylation of ribulose bisphosphate catalyzed by ribulosebisphosphate carboxylase from *Rhodospirillum rubrum*. *Biochemistry*, 24, 1603–1607.

Rothpletz, A. (1892). On the formation of oolite. *American Geologist*, 10, 279–282.

Rupke, A. L., & McDonald, A. (2012). *Great Salt Lake brine chemistry database, 1966–2011. Utah Geological Survey Open-File Report 596*. Salt Lake City, UT: Utah Department of Natural Resources.

Sei, A., & Fathepure, B. Z. (2009). Biodegradation of BTEX at high salinity by an enrichment culture from hypersaline sediments of Rozel Point at Great Salt Lake. *Journal of Applied Microbiology*, 107, 2001–2008.

Shiraishi, F., Hanzawa, Y., Okumura, T., Tomioka, N., Kodama, Y., Suga, H., ... Kano, A. (2017). Cyanobacterial exopolymer properties differentiate microbial carbonate fabrics. *Scientific Reports*, 7, 1–8.

Spero, H. J., Andreasen, D. J., & Sorgeloos, P. (1993). Carbon and nitrogen isotopic composition of different strains of *Artemia* sp. *International Journal of Salt Lake Research*, 2, 133–139.

Steinman, B. A., Abbott, M. B., Nelson, D. B., Stansell, N. D., Finney, B. P., Bain, D. J., & Rosenmeier, M. F. (2013). Isotopic and hydrologic responses of small, closed lakes to climate variability: Comparison of measured and modeled lake level and sediment core oxygen isotope records. *Geochimica et Cosmochimica Acta*, 105, 455–471.

Stolper, D. A., & Eiler, J. M. (2015). The kinetics of solid-state isotope-exchange reactions for clumped isotopes: A study of inorganic calcites and apatites from natural and experimental samples. *American Journal of Science*, 315, 363–411.

Talbot, M. R. (1990). A review of the palaeohydrological interpretation of carbon and oxygen isotopic ratios in primary lacustrine carbonates. *Chemical Geology: Isotope Geoscience Section*, 80(4), 261–279.

Trower, E. J., Lamb, M. P., & Fischer, W. W. (2017). Experimental evidence that ooid size reflects a dynamic equilibrium between rapid precipitation and abrasion rates. *Earth and Planetary Science Letters*, 468, 112–118.

Vázquez-Baeza, Y., Pirrung, M., Gonzalez, A., & Knight, R. (2013). EMPor: a tool for visualizing high-throughput microbial community data. *GigaScience*, 2(1). <https://doi.org/10.1186/2047-217X-2-16>

Visscher, P. T., Reid, P. R., & Bebout, B. M. (2000). Microscale observations of sulfate reduction: Correlation of microbial activity with lithified microcritic laminae in modern marine stromatolites. *Geology*, 28, 919–922.

Visscher, P. T., & Stolz, J. F. (2005). Microbial mats as bioreactors: Populations, processes, and products. *Palaeoclimatology, Palaeoecology*, 219, 87–100.

Walsby, A. E., Van, R. J., & Cohen, Y. (1983). The biology of a new gas-vacuolate cyanobacterium, *Dactylococcopsis salina* sp. nov., in Solar Lake. *Proceedings of the Royal Society of London - Biological Sciences*, 217. <https://doi.org/10.1098/rspb.1983.0019>

Wright, D. T. (1999). The role of sulphate-reducing bacteria and cyanobacteria in dolomite formation in distal ephemeral lakes of the Coorong region, South Australia. *Sedimentary Geology*, 126(1–4), 147–157.

Zeikus, J. G. (1983). Metabolic communication between biodegradative populations in nature. In *Society of General Microbiology Symposium 34 Proceedings* (pp. 423–462).

Zhong, Z. P., Liu, Y., Wang, F., Zhou, Y. G., Liu, H. C., & Liu, Z. P. (2016). *Psychroflexus salis* nov., sp. nov. and *psychroflexus plancticus* nov., sp. nov., isolated from a salt lake. *International Journal of Systematic and Evolutionary Microbiology*, 66(1), 125–131.

## SUPPORTING INFORMATION

Additional supporting information may be found online in the Supporting Information section.

**How to cite this article:** Ingalls M, Frantz CM, Snell KE, Trower EJ. Carbonate facies-specific stable isotope data record climate, hydrology, and microbial communities in Great Salt Lake, UT. *Geobiology*. 2020;00:1–28. <https://doi.org/10.1111/gbi.12386>